Green synthesis of nanoparticles

Dissertation

zur Erlangung des akademischen Grades
Doktor der Ingenieurwissenschaften
(Dr.-Ing.)

der Technischen Fakultät
der Christian-Albrechts-Universität zu Kiel

Duygu Disci-Zayed

Kiel

December 2015

1. Gutachter

Prof. Dr. Mady Elbahri

2. Gutachter

Prof. Dr. Lorenz Kienle

Datum der mündlichen Prüfung

29.04.2016

To my son

Abstract

There are many definitions for nanotechnology and nanomaterials due to their multidisciplinary nature. The general definition of nanomaterials is that the structures have at least one dimension in the range of 100 nm or smaller. The definition for nanotechnology is that it is a discipline to investigate the production, manipulation, design, and engineering of nanomaterials. The use of nanomaterials has been spread in a large palette of applications such as energy, optics, electronic and medicine. Nowadays the state of the art nanoscience is capable of producing many multifunctional materials, however they have shortcomings such as using hazardous chemicals, methods being complicated and cost intensive and lack of scalability. In order to eliminate this shortcomings green synthesis techniques have been evolved recently.

Green syntheses are environmental friendly alternatives to conventional synthesis techniques. They aim to reduce toxic elements used or produced in conventional methods. Moreover, they benefit from sustainable sources and can reduce production cost, in practical and up-scalable manner.

In this thesis we focus on two different green synthesis techniques. In our first technique, silver/gold plasmonic bionanocomposites (BNCs) as well as 3D bio-shells decorated with BNCs are produced using natural products in a biogenic fashion. In such techniques biomolecules such as enzymes, proteins, bacteria, fungus, yeast, and plant biomasses, are used to produce nanoparticles. The produced particles are highly promising for biological applications due to their biocompatible nature.

Our second technique is based on Leidenfrost phenomenon where Leidenfrost dynamic chemistry occurring in an underwater overheated confined zone is used as a smart, versatile and a quick way of zinc peroxide nanoparticle production. The produced particles are then investigated in terms of cytotoxicity effect on cancer and healthy cells to prove their applicability as cancer nanotherapeutics.

Table of Contents

List of Figures

List of Tables

Preface:

There are many definitions for nanotechnology and nanomaterials due to their multidisciplinary nature. The general definition of nanomaterials is that the structures have at least one dimension in the range of 100 nm or smaller. The definition for nanotechnology is that it is a discipline to investigate the production, manipulation, design, and engineering of nanomaterials. The use of nanomaterials has been spread in a large palette of applications such as energy, optics, electronic and medicine. During last decades, nanotechnology was considered as an emerging field of science especially in biological applications [1], [2].

Nanoparticles have attracted huge attention in biological applications promptly. As the size of the particles reduces, their surface area-to-volume ratio rapidly increases. Accordingly, such an extensive surface area offers larger active sites which can be engineered and decorated to optimize functionality, solubility, and biocompatibility. At this size range, materials behave differently compared to their bulk counter parts. Unusual chemical, electrical, magnetic, and optical properties emerging at these dimensions make them potential candidates for sensoric, therapeutic, and diagnostic applications. Additionally, nanoparticles are in the same dimensional scale of biological media, thus offering a great advantage for their integration into biological systems [3].

Today we are accustomed to hear the word 'nano' along with biology, however, the realization of biological applications of nanoparticles *in vitro* or *vivo* has never been an easy task. First of all, the nanoparticles to be used should be biocompatible, or able to be biocompatiblized. Secondly their production methods should be simple, non-hazardous, inexpensive, and upscalable for a wide range of applications. The surface imperfections and impurities of the product in general increase with the complicity of the nanofabrication technique. Thus, the product will be less likely biocompatible. Although nowadays the state of the art nanoscience is capable of producing many multifunctional materials for health care systems, the shortcomings mentioned above hinders their commercialization and many of them remain in laboratory scale. Biological applications are associated with human life, thus require very sensitive systems able to perform perfectly.

Fortunately, in the last decades, scientists have considered natural sources as raw materials to eliminate the toxicological and hazardous effects of chemicals used in synthesis and to reduce the production cost simultaneously. This tendency has induced employment of green synthesis

techniques in nano-bioscience. Green syntheses are environmental friendly alternatives to conventional synthesis techniques which benefits mainly from the extraordinary features of natural sources. Within this thesis we used biogenic synthesis where biomolecules such as enzymes, proteins, bacteria, fungus, and yeast as well as plant biomasses were used to produce nanoparticles. The materials synthesized in this way are absolutely suitable for biological applications, such as recognition and therapy of cancers. For instance, noble metal nanoparticles, such as gold and silver, are used due to their plasmonic properties mainly for detection purposes. Furthermore, magnetic nanoparticles are employed especially in therapy such as hyperthermia [4], [5].

In this thesis a novel, simple, and low cost green synthesis technique is introduced to produce silver/gold plasmonic bionanocomposites (BNCs) as well as 3D bio-shells decorated with BNCs using silk cocoons. The produced particles are highly promising for biological applications due to their biocompatible nature.

1. Introduction

Nanomaterials are becoming attractive in biological applications mainly because of their comparable size to biological media. In addition, possessing a very large surface area-to-volume ratio makes them active building blocks that can be decorated with various drugs and functionalized with various functional groups. The nanomaterials have been used as tiny sensors to analyze and to detect diseases, as communicating agents between organisms or for therapy purposes to treat various health problems. Due to their broad application palette nanomaterials have made an outstanding progress in biological applications [1], [2].

Today's technology is capable of giving various functions to nanomaterials, however, many of them remains only at laboratory scale and cannot be commercialized mainly due to complexity of the synthesis procedure, high cost, and poor biocompatibility. In order to improve biocompatibility, nanoparticles should be coated with biopolymers and/or antibodies or contrarily the toxic ligands attached should be removed by a post synthesis process. In the both cases the post synthesis process increases the cost as well as the production time. Such challenges necessitate seeking alternatives for the conventional synthesis protocols. Nowadays, especially for medical applications, green synthesis techniques are going to be used extensively. Based on its definition many synthesis techniques could be considered as green methods. In this thesis we attribute the name of 'green' to those synthesis approaches providing high yield of biocompatible products with cost and energy efficiency.

The wide range of nanoparticles used in medicine includes those made from metals, polymers, and ceramics. This study focuses on metallic nanoparticles due to their intrinsic optical properties and healing processes. Dating back to ancient times silver, copper, and gold, whether as bulk or nano used as decorations, or employed as antimicrobial agents. Noble metal nanoparticles can be synthesized via various methods commercially. Nevertheless, synthesizing them for a medical application is not an easy task due to the reasons mentioned above. In order to overcome the involved problems, green synthesis methods could be proper alternatives. Next chapters will focus on the conventional and green synthesis methods to produce gold and silver nanoparticles. Later on, the properties of silk and its role in the green synthesis will be explained. In the following sections, the existing studies related to reduction of metal salts via silk proteins will be presented. Furthermore, our new approach that is able to produce plasmonic bionanocomposites with high

yield by using reduction ability of bio entities of silk will be introduced. Moreover, mainly due to the outstanding plasmonic properties of the products, their potential medical applications will be probed. The synthesis characterizations were mainly performed by using fluorescence spectroscopy due to the existence of intrinsic fluorophores.

1.1 Silver nanoparticle synthesis and applications

The use of silver dates back to ancient times. In this era, civilizations such as Greeks, Egyptians, Romans and Phoenicians used silver utensils to protect their water and food from spoiling. Even Hippocrates, the father of the medicine, who lived between 460-370 B.C. treated wounds and ulcers by using silver containing mixtures [6]. Later in history we have seen application of silver in the medieval stained glass or Lycurgus cup, conferring its well-known yellow to green hue when used as nanoparticles [7], [8]. Nowadays, silver nanoparticles are well known materials in high tech applications such as conductive inks and photonic devices. Additionally, due to their antibacterial capability they are frequently used in medical industry and in household appliances.

Silver nanoparticles are conventionally synthesized through chemical methods. In such approaches, silver ions (Ag^{+}) from different silver salts are reduced by citrates and-or borohydrates, forming atomic silver (Ag^{0}). The atomic silver is aggregated as nano clusters. Nanolclusters` size and stability is tuned by stabilizing/capping agents [9].

Silver nanoparticles are particularly efficient at absorbing and scattering light which occurs due to surface plasmon resonance. Depending on their size and electronic properties, silver nanoparticles have surface plasmon resonance absorption in the range of 400-530 nm [10].

1.2 Gold nanoparticle synthesis and applications

Similar to silver, the potential applications of gold were also discovered in ancient times. The use of ruby medieval glass and red hue in Lycurgus cup are also common examples to the use of gold nanoparticles [7], [8].

The most common and well known synthesis technique of gold is known as “Turkevich” technique. This method was later modified by Frens and is known today as “Turkevich- Frens” method. The technique is based on reduction of gold hydro chlorate solution by citrate at 100°C. Here, citrate ions act as stabilizing and reducing agents simultaneously. The particle size of the

obtained nanoparticles varies in the range of 10-50 nm. One disadvantage of his technique is the poor surface chemistry of the resulted particles due to easy degradation of citrates [9].

Another preparation technique of gold nanoparticles is known as “Brust-shifferon” method which is a two phase method to produce thiol stabilized gold nanoparticles in organic solvents. Compared to the previous technique, this method gives rise to formation of relatively smaller nanoparticles in the range of 2-2.5 nm. The made nanoparticles are also more stable for a longer time [11], [12]. An alternative to the both techniques could be laser ablation where a bulk gold plate is irradiated with a plasma plume generated by laser [13].

The surface plasmon resonance wavelength of gold nanoparticles, depending on their size and shape, varies between 500-600 nm. For instance, 50 nm spherical gold nanoparticle would show a surface plasmon resonance peak at 520 nm [14].

1.3 Silk cocoons of Bombyx mori silk worm

Silk cocoons secreted by Bombyx mori silk worm are composed of two main proteins: fibroin and sericin. They possess a core-shell structure, whose core is in fact twinned fibroin fibrils (70% of the cocoon) encompassed by the glue like sericin protein (30% of the cocoon). A thin layer of water soluble glycoproteins named seroin surrounds the sericin proteins [15]. Fibroins are composed of high (350 kDa) and light (29 kDa) chain proteins connected by a glycoprotein called P25 and disulphide bonds [16]. They consist of highly crystalline β-sheets and less or non-crystalline phases. Sericin, on the other hand, having polypeptides with molecular weight ranging from 24 to 400 kDa, consists of 35% β-sheet and 63% random coil structure without any α-helical structure. The amino acid compositions of fibroin and sericin show similarities, as shown in Table 1. A notable difference is the predominance of polar amino acids such as serine, aspartic, and glutamic acid which confer a hydrophilic nature to sericin. Fibroin, elsewise, is mainly made of non-polar amino acids such as glycine and alanine offering the protein hydrophobic properties.

1.4 Silk sericin and its applications

Sericin is long being treated as a worthless byproduct and has been removed from cocoons via a degumming process. Its molecular weight changes between 8 [17] to 350 kDa [18]. Two major genes encoding for sericin are Ser1 and Ser2 [15]. Ser2 is thought to be the responsible gene for adhesive properties of sericin. This gene is rich in tyrosine, possessing the strong sticking group of amino acid 4-hydroxyphenylalanine [19]. It is assumed that, in analogous to the mussel,

hydroxyphenylalanine in sericins provides the adhesion ability to a wet surface through a crosslinking reaction under water [20]. Due to its hydrophilic nature, in presence of alkalis residues of low (~20 kDa) and high molecular weight sericins are dissolved in cold and hot water, respectively.

Table 1 Amino acid compositions of sericin and fibroin (residues/1000 of hydrolysis product) [21]**.**

Amino Acid	Sericin	Fibroin
Aspartic Acid	148	13.3
Threonine	86	9.2
Serine	373	121.3
Glutamic Acid	34.1	10.2
Proline	7.6	3.1
Glycine	147	445.3
Alanine	43	293.5
Valine	35.4	22.4
Cystine/2	5.1	-
Isoleucine	7.6	7.1
Leucine	13.9	5.1
Tyrosine	25.3	52
Phenylalanine	3.8	6.1
Lysine	24	3.1
Histidine	11.4	1.6
Arginine	35.4	4.6
Tryptophan	-	1.5

In some studies sericin has been described as a layered structure having fractions of sericin I (A,α), II (B,β), and III (C,γ) from outer to inner layers, respectively, covering twinned fibroins. Each fraction has different degree of solubility. In addition to the crystalline phases sericin A, the most soluble one, has an amorphous structure. The rest have relatively low solubility and are found in the crystalline form. Despite its solubility, sericin undergoes gelation at room temperature above a concentration of 5% [15], [17], [18], [22].

In recent studies, sericin has been highlighted for medical, pharmaceutical, and cosmetic applications mainly due to its moisturizing, antioxidizing, UV- protecting, dietary, and anticoagulant properties. Despite contradicting opinions, sericin is believed to cause no

inflammatory activity in its soluble form. Its high content of hydroxyl amino acids, offering an antioxidant property, makes it a valuable additive in food and cosmetics. Additionally, suppressing the oxidative stress, it overwhelms the chemical as well as UV radiation induced skin tumorigenesis. It is also used as a supplement in serum free media for proliferation of different mammalian cells [15].

1.5 Green synthesis of silver and gold nanoparticles

Green syntheses are environmental friendly alternatives to conventional synthesis techniques. They aim to reduce toxic elements used or produced in conventional methods. Moreover, they benefit from sustainable sources and can reduce production cost, in practical and up-scalable manner. In this thesis we focus on biogenic synthesis which uses biomolecules such as enzymes, proteins, bacteria, fungus, yeast, and plant biomasses, to produce nanoparticles. Reduction of nanoparticles can be done through enzymatic or non-enzymatic as well as intracellular or extracellular reactions (the latter in case of using living organisms). While enzymatic reactions are slow non-enzymatic reactions are relatively faster processes. The latter kind of reactions are also controlled by pH and temperature; thereby nanoparticle parameters, *e.g.*, size and shape can be adjusted [18], [22]. Some examples of the synthesized nanoparticles using biomolecules-entities can be seen in Table 2.

1.6 Green synthesis of silver and gold nanoparticles using silk sericin

One of the first studies on sericin-silver interactions was presented by Bhat *et al.* [23]. They used sericin as a stabilizing agent which was prepared by boiling of 2 g of the cocoons in 200 mL purified water. Then they filtered the solution to remove the gelatinous precipitates and finally sonicated the filtrate. They noted the absorption spectrum of this solution at 276 nm, *i.e.* the typical absorption spectrum of aromatic amino acid Tyr residues [23]. Silver nanoparticles were prepared by mixing 100 mL of 0.29 mM silver nitrate solution with 0.5 mL of 0.01 M sodium borohydrate at constant stirring. The nanoparticles were made instantly. The relevant absorption spectrum was recorded at 389 nm, proving formation of silver nanoparticles. The reduced particles were mixed with 3% by volume sericin solution and another UV-Vis measurement performed. The UV-Vis spectrum of the stabilized solution showed the absorption peak at 399 nm, confirming the capping of silver nanoparticles.

Table 2 Biogenic synthesis via different bio products (modified from [18]**).**

Bio product	Synthesized nanoparticle	Particle size	Reference
Aloe vera (Plant)	Ag	15.2 ± 4.2 nm	Chandran *et al.* (2006)
Aspergillus fumigatus (Fungus)	Ag	5–25 nm	Bhainsa and D' Souza (2006)
Colletotrichum sp. (Fungus)	Au	20–40 nm	Shankar *et al*. (2003a)
Emblica Officinalis (Plant)	Ag and Au	(10–20 nm) and (15–25 nm)	Ankamwar *et al*. (2005a)
Pseudomonas aeruginosa (Bacterium)	Au	15–30 nm	Husseiny *et al.* (2007)
Cinnamomum camphora (Plant)	Au and Ag	55–80 nm	Huang *et al.* (2007)

They explained stabilization mechanism both steric and electrostatic means. The suggested electrostatic repulsion, responsible for steric stabilization, could occur between the negatively charged sericin micelles and hydrophilic lateral groups of sericin.

Another important study was published by Nivedita *et al.* [24]. They used sericin as the capping and reducing agent. They employed the same technique and concentration of sericin solution as described by Bhat *et al.* [23]. Sericin was blended with 10^{-3} M silver nitrate solution at 40^{o}C in equal volumes at constant stirring. They heated this mixture up to 60^{o}C and adjusted the pH to 8.5 with 5% NaOH in order to increase the solubility of sericin. After a reaction time of 48 hours the yellow plasmonic color of silver nanoparticles as well as absorption band at 415 nm were observed. In this reaction, NaOH acted as a catalyst. They repeated the same experiment in absence of NaOH and observed the NP generation at a slower rate resulting in bigger particles with larger size distribution. The exact mechanism of reduction was not clarified, however, they stated that the absorption peak of sericin at 275 nm, which can be attributed to Tyr residues, has been vanished during the NP synthesis indicating its consumption and contribution to reduction and capping mechanism [24].

Ding and Wu [25] presented similar but an extended research about capping and reducing capability of sericin in presence of silver nanoparticles. They used commercial sericin with 10

mol/L dissolved in triple distilled water. In their experiment 5 mL $AgNO_3$ (1 mmol/mL) was mixed with 5 mL of sericin solution (10 mol/L) stirred until the solution was homogeneous with a pH of 9. At that pH a yellow brownish colloidal solution was obtained after 7 days at room temperature. Two more colloids were prepared by adjusting the pH of the solution to 7 and 5 [25]. As a simple and useful tool they also analyzed the samples with UV-Vis spectrometer. The absorption of 10 mM sericin was recorded at 275 nm which can be attributed to π-π* electron transitions from aromatic amino acids Tyr, Phe, and Trp. After the synthesis, they observed that the peak at 275 nm has been diminished and the peak at 424 nm appeared indicating silver NP generation. The strongest reducing capacity of the stated amino acids belongs to Tyr. That is why they assumed the reaction as follows: phenolic group of the Tyr is ionized and transformed to quinone by electron transfer to silver ions as shown in Figure 1. Different NP yields have been observed at various pH conditions. Production at pH 5, showed almost a clear solution as well as no absorption peak in UV-Vis spectrum. Colloidal solution at pH 7, on the other hand showed a peak at 394 nm and a yellow solution. The production at pH 9 presented the highest yield with a reddish color and an absorption spectrum at 424 nm.

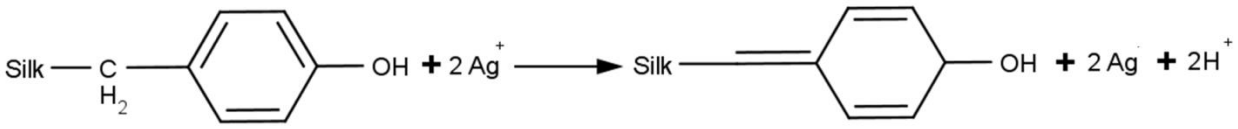

Figure 1 Tyr ionization (modified from [25]**).**

At alkaline conditions phenols undergo deprotonation creating phenolate anions. The anions transfer electrons to the silver ions thereby forming metallic silver and transform the structure to a semi-quinone structure. Accordingly, when pH increases protons are neutralized by NaOH, and the redox potential of the reducing agent is increased. pH recording after 7 days also showed pH value declines. This is a good proof of the H^+ generation confirming their assumption.

In a very recent study, Aramwit *et al.* [26] used sericin as the capping and reducing agent and synthesized silver nanoparticles in the range of 48-117 nm at pH 11. They used different concentrations of sericin and $AgNO_3$ to investigate the effect of each parameter.

In this study, sericin was first degummed via a high temperature and pressure technique and then filtrated through a filter paper to remove fibroin residues. Remaining sericin solution was

concentrated until the desired concentration was achieved (approximately 7 wt%) and used as a stock solution which was then diluted to concentrations of 5, 10, and 20 mg/mL. The pH values in all the cases were kept at 9 and 11 (adjusted via NaOH addition). The prepared sericin solutions were subsequently blended in 1:1 proportion with 1, 5 and 10 mM of $AgNO_3$ solutions under constant stirring. All mixtures were stirred overnight at room temperature. After sufficient time, the solutions became yellowish indicating Ag nanoparticles formation. The authors of this study, investigated the effects of pH and concentrations of $AgNO_3$ along with silk sericin concentration on the formation of sericin capped silver nanoparticles using UV-Vis spectroscopy. According to their results, while the samples produced at pH 9 showed no particle formation, the plasmonic peak at 420 nm as well as the plasmonic color were observed only in the mixtures prepared at pH 11. The yield of the samples was completely dependent on the $AgNO_3$ concentration rather than the sericin's. To elaborate the involved reducing and capping mechanisms, they performed Fourier transform infrared spectroscopy **(**FT-IR**)** analyses. Their data showed that carboxylate groups from alkaline degradation of sericin act as a reducing agent while COO^- and NH_2^+ groups would stabilize the generated silver nanoparticles [26].

Despite numerous detailed researches about the reducing mechanism of silver nanoparticles, similar studies for gold nanoparticles can only be found in presence of fibroin. Since sericin and fibroin have a similar type of amino acid groups, the reduction mechanism could be the same and based on phenyl groups of aromatic amino acids.

1.7 Intrinsic fluorophores

Intrinsic fluorophores, such as tryptophan (Trp), tyrosine (Tyr), phenylalanine (Phe), NADH, Pyridoxal, and their derivatives, have played an important role in exploring our synthesis method. Tyr, Trp, and Phe fluorescence due to possession of aromatic groups and in water show emission at 304 nm, 353 nm and 282 nm, respectively. Among them in most cases, energy transfer from Tyr to Trp or interactions between peptide chains quench the Tyr emission. Furthermore, due to its weak fluorescence Phe is mostly superimposed by the Tyr and Trp emissions. Emission maxima of Tyr and Phe are independent from the local environment. Yet, Trp is prone to local changes which would contribute to conformational transitions. While judging the emission maximums of natural fluorophores one should be careful. Tyr for example might go through excited-state ionization and forms tyrosinate which shows emission wavelength similar to Trp at 350 nm. Phenolic OH groups are expected to be ionized at alkaline pH environment. That is why tyrosinate

transformation is mostly observed at higher pH values except in the presence of acetates as proton acceptors where the reaction can take place at neutral pH values [27]. Emission spectra of Tyr at different pH values can be seen in Figure 2.

Enzymes such as NADH which is formed through electron transfer to NAD^+ show an emission around 460 nm. When excited, this emission occurs at 340 nm due to the reduced nicotinamide rings. Yet, its oxidized form NAD^+ shows no fluorescent [27].

Another intrinsic fluorophore is Pyridoxal which is a cofactor and one form of vitamin B6 [28]. Pyridoxal has a complex structure and its emission wavelength shows variations depending on its chemical structure. Two major derivatives of this coenzyme are pyridoxyl phosphate and pyridoxamine. The former one shows alterations in the emission spectrum depending on its interactions with other proteins. The latter one is dependent on pH values. An overview to emission and excitation values of natural fluorophores can be seen in Figure 3 [27].

Bionanocomposites attached with intrinsic fluorophores can be used to detect ions due to fluorescence quenching. Quenching mechanisms might be complicated and for better understanding a brief relevant introduction will be presented.

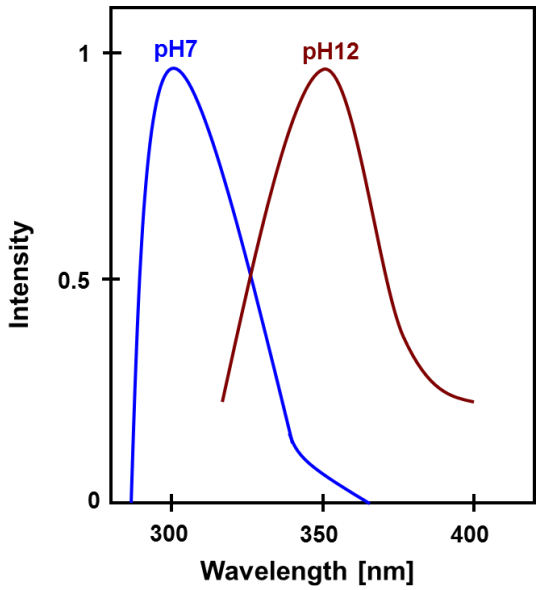

Figure 2 Tyrosine emission spectra at different pH values (modified from [27]**).**

Intrinsic fluorophores can be quenched due to exposure to environmental changes. This property can be used in sensoric applications. In the following chapter fluorescent quenching will be briefly explained.

1.8 Fluorescence quenching and its application in ion detection

A decrease in the fluorescence intensity is referred as fluorescence quenching and occurs due to molecular interactions such as energy transfer, molecular rearrangements, and collisional quenching [27]. In this work we will consider two involved mechanisms: dynamic and static quenching. The former one arose due to the collision encountering between the quencher and fluorophores. In this case, the quencher diffuses into the fluorophore within the life time of the excited state and the fluorophore returns to its ground state without emission of a photon. The latter one occurs in case of binding between fluorescent samples and the quencher resulting in a non-fluorescent complex. Both mechanisms require an interaction between fluorophores and the quencher. This fact can be a very useful tool to identify protein-membrane structures. The well-known quenchers are molecular oxygen, heavy atoms, purines, and pyrimidines. Quenching data are presented classically by quantification of fluorescence intensities in the absence (F_0) and presence (F) of a quencher versus concentration ([Q]) of the quencher.

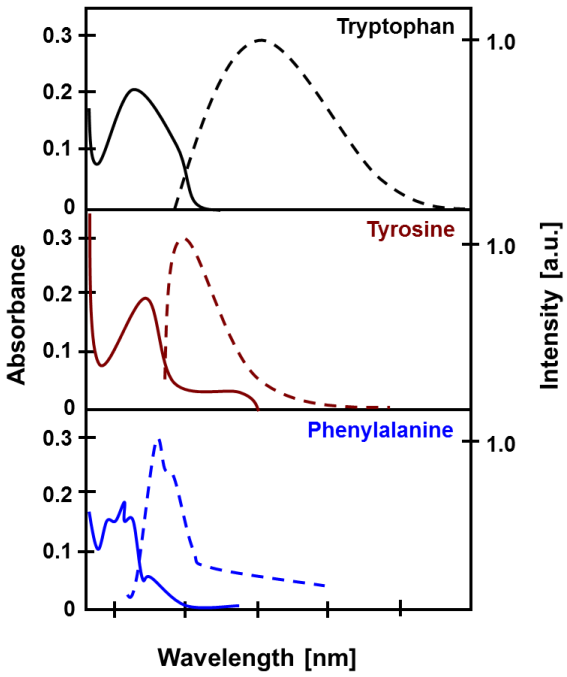

Figure 3 Emission and absorption spectra of Tyr, Trp and Phe (modified from [27]**).**

1. Introduction

Dynamic quenching can be described through the Stern-Volmer equation below:

Equation 1

$$\frac{F_0}{F} = 1 + k_q \tau_0 [Q] = 1 + K_D [Q] \qquad [27]$$

In this equation k_q, τ_0, and K_D are biomolecular quenching constant, lifetime of the fluorophores in the absence of quencher, and Stern-Volmer constant, respectively.

Static quenching is described by Equation 2 and Equation 3 where [*F*], [*Q*], and [*F*-*Q*] represent concentration of the uncomplexed fluorophores, concentration of the quencher, and concentration of the complex, respectively.

Equation 2

$$\frac{F_0}{F} = 1 + K_S [Q] \qquad [27]$$

K_s which is the Stern-Volmer constant for static quenching is given by Equation 3.

Equation 3

$$K_S = \frac{[F-Q]}{[F][Q]} \qquad [27]$$

Recalling $[F]_0$ total fluorophores concentration given by Equation 4.

Equation 4

$$[F]_0 = [F] + [F - Q] \qquad [27]$$

Substitution of Equation 4 into Equation 3 will give us Equation 5 for static quenching.

Equation 5

$$K_S = \frac{[F]_0 - [F]}{[F][Q]} = \frac{[F]_0}{[F][Q]} - \frac{1}{[Q]} \qquad [27]$$

After proper arrangements the final equation for static quenching is given by

Equation 6

$$\frac{F_0}{F} = 1 + K_S[Q] \qquad [27]$$

As seen from both Equation 1 and Equation 6 the ratio of F_0/F on $[Q]$ is linear in both quenching mechanisms.

Such linear ratio implies that solo intensity measurement in absence of any other information is not conclusive to determine the quenching mechanism. The most accurate way to determine it would be the measurement of fluorescence lifetimes. Another method to distinguish quenching mechanism could be done through careful measurements of absorption spectra of the fluorophore. Since dynamic quenching affects only the excited state of the fluorophores no change in the absorption spectra is expected. Additionally, dynamic quenching can be also distinguished through its temperature dependence. Since higher temperatures lead to faster diffusion larger magnitude of dynamic quenching is expected when temperature rises [27].

In some cases, the both mechanisms might coexist. This co-existence will result in an upward curvature in the Stern-Volmer plots. In this case a modified approach of the Stern-Volmer equation which is second order in [Q] is needed and accounts for the concave curve towards *y*-axis.

The modified equation is represented as Equation 7, wherein F_0 and the F are given by the product of the fraction that is not complexed and the fraction that is not quenched by collisions.

Equation 7

$$\frac{F_0}{F} = (1 + K_D[Q])(1 + K_S[Q]) \qquad [27]$$

1.9 Plasmonic nanoparticles

The name of plasmonic comes from the word ‘plasma’ which is a medium owning freely mobile charges. Their interaction with light results into resonant modes, also known as plasmons. Finally, plasmonic is described as a division of optics which studies the collective oscillations of conduction electrons of plasma [29].

1. Introduction

Nanoparticles show intrinsic plasmonic properties due to their changing size, shape and composition. These properties are dominated with collective oscillations of the conduction electrons which are triggered through electromagnetic radiations. Due to their high amount of free conduction electrons Au, Ag, and Cu are mostly used in plasmonic applications. Briefly if nanoparticles are irradiated by visible or infrared light electrons of nanoparticles oscillate coherently due to the electric field conduction resulting in a unique resonance wavelength. This unique wavelength is influenced greatly by the size, shape, and composition (dielectric constant) of the nanoparticles as well as their surrounding media [30].

An example of the effect in particle shape, size, and composition on to plasmonic properties is shown in Figure 4. In Figure 4a, b, and c TEM micrographs of Au nanospheres, nanorods, and Ag nanoprisms, respectively, are shown. Figure 4d, e, and f show the colloidal dispersions having different plasmonic colors due to changes in Au-Ag concentrations, aspect ratios, and lateral size of nanoparticles. Section d belongs to Au-Ag alloy nanoparticles with increasing Au concentration. In Figure 4e Au nanorods are shown with increasing aspect ratios and finally in section f we see the effect of increase in lateral size of nanoprisms on plasmonic properties of the nanoparticles.

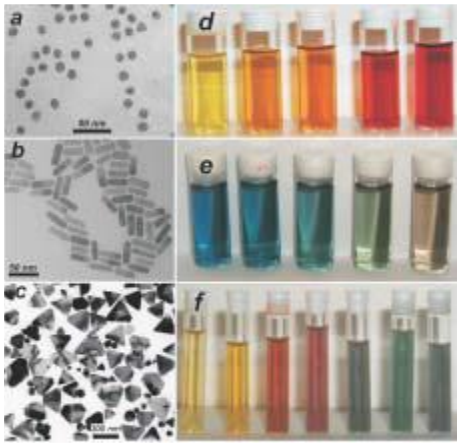

Figure 4: Transmission electron micrographs of Au nanospheres (a) and nanorods (b) and Ag nanoprisms (c, mostly truncated triangles) formed using citrate reduction, seeded growth, and DMF reduction, respectively. Photographs of colloidal dispersions of AuAg alloy nanoparticles with increasing Au concentration (d), Au nanorods of increasing aspect ratio (e), and Ag nanoprisms with increasing lateral size (f). Figures reprint from reference [30] **with permission (License number- 3761561311778, Elsevier 2004).**

As stated in the previous chapter, the first applications of silver and gold nanoparticles date back to ancient times, *e.g.*, in medieval church windows. Today, we use them far beyond aesthetic

purposes and in more functional and advanced applications such as in solar cells, bio detection, sensors, and cancer therapy. As one of the most interesting and important application areas, some potential application of biomedical sensors will be introduced in this thesis.

1.10 Green synthesis via the Leidenfrost Effect

The Leidenfrost phenomenon is an old scientific concept. However, its implementation to create smart materials and functional systems were shown in a recent study [31]. According to this phenomenon, if a drop of liquid is placed on a hot surface having much higher temperature than the liquid's boiling point the droplet will hover on a vapor cushion due to very fast evaporation. Thanks to the vapor cushion beneath the droplet acting as an insulator, the droplet remains on the hot plate longer than several minutes instead of evaporating in seconds. During the fast evaporation of water, as observed by several scientists' centuries ago, the water shows diverse characteristics in terms of charge separation and self-ionization [31].

Despite no already quantitative representation, under rapid evaporation conditions, generation of a positively charged steam has been clearly verified. R. Abdelaziz *et al.* also proved its validity to a Leidenfrost drop [31]. In this experiment, a tungsten tip which can be adjusted in height was attached to a grounded electrometer in order to measure the charges within the Leidenfrost drop as well as the vapor layer around it. As the heating surface, an aluminum plate connected to a grounded heating unit was used. In order to eliminate any charging effect, an insulating layer was placed between the heating unit and the aluminum layer and all the units of the setup were placed in a closed lab-built apparatus controlled by the National Instruments LabView software.

It was found out that as the cold droplet was poured on to the hot surface at 250°C, no charges were recorded at this instant second. However, from the time of the steam generation until the levitated state, negative charges increased constantly until reaching to a saturation value.

This experiment was repeated at ambient as well as boiling temperatures of water and no charge generation at any stage of the experiment was observed. Such an observation proved the important contribution of fast evaporation to charge separation, as shown previously by Shaw, Lenard [32] and Gilbert and Shaw [33]. Contrarily, their recording for the vapor layer above the droplet showed positive charges. Since the salt solutions can attack to hydrogen network of water and favor self-ionization, the charges of the salt solutions at different concentrations are monitored instead of

water. Expectedly, recorded charges were equivalently increased for higher salt concentrations. It is suggested that self-ionization of water will be in a way that the increase of the hydroxide ions due to self-ionization will enhance the local pH value of the droplet. Increased amount of hydroxide ions would not only favor some chemical reactions but also can act as a reducing agent.

As a conclusion, the Leidenfrost drop itself acts as a chemical reactor where one can tune pH of the environment and ease the nanoparticle formation of many substances by hydroxide ions' reducing ability. Based on this technique gold, zinc oxide, and copper oxide nanoparticles have been successfully produced [31].

1.10.1 Green synthesis of zinc oxide nanoparticles via Leidenfrost phenomenon

Relying the Leidenfrost phenomenon star like and spherical ZnO and ZnO_2 nanoparticles have been synthesized through our green synthesis technique.

The Leidenfrost phenomenon driven synthesis method established in our work is very versatile in synthesizing zinc oxide and zinc peroxide nanoparticles in minutes. In this technique, we have used very simple equipment such as regular hot plates and glass beakers, as well as very cost effective materials *i.e.* water as the solvent and zinc peroxide as precursor, and NH_4OH and H_2O_2 to adjust pH values and as oxidizing agent respectively. Water, due to collision of its molecules, shows a self-ionization effect; thereby hydronium and hydroxide ions are formed. As stated in the previous chapter, the amount of hydroxide ion is crucial in our experiments in order to increase the local pH and to act as a reducing agent.

All the experiments of this work were carried on a hot plate heated to 300^{o}C. This temperature was chosen to create a vapor film at the glass (beaker)-liquid interface, mimicking the conditions of the Leidenfrost effect. Rapid vaporization events occurring at the interface contribute to an equally paced formation of nanoparticles at very short time through convection of heat, supplying the necessary activation energy for nucleation of nanoparticles.

This novel technique can be manipulated in order to synthesize nanoparticles of different morphologies, chemistries, and sizes by slight pH adjustments, addition of oxidizing agents as well as by changing the experiment media. In the synthesis, no toxic chemicals or surfactants were used. Accordingly, the product has an optimum potential for biological applications. In the present study the nanoparticles were investigated for possible cancer therapies.

1.11 Biological applications of nanoparticles

Nanoparticles offer many advantages in biological researches. Nanoparticle systems composed of polymer, metal, or metal oxides possess intrinsic electronic, optical, and structural properties compared to their bulk forms. On top of that their small size comparable to biological entities makes their integration into biological systems easier. Moreover, supplying a higher surface area-to-volume ratio makes them potential substrates for surface functionalization with various pharmaceuticals, proteins, and ligands for increased efficiency, solubility, stability, and biocompatibility. Some of their important applications include: biological labels, drug delivery systems, anti-cancer therapies, detection of bio-molecules, and MRI contrast agents [3], [34]. Even though each individual application deserves more explanation and admire the present study focuses on cancer therapy.

Cancer is a very complicated disease having dozens of types each showing divergence symptoms and reactions from one patient to other. Such diversity makes its diagnosis and treatment intricate. Depending on the type, location, and size of the cancerous area different treatment methods are available where the most common one is the chemotherapy. Cancer cells are abnormally divided at high pace due to different environmental factors and mutations of the cell DNAs. The chemotherapeutical agents are designed to attack to fast growing cells without differentiating healthy and malignant cell population. This incapability could be problematic and lead to systematic toxicity and adverse side effects [34].

To overcome this problem, nanoparticle of different kinds (metal, semiconductor, polymer, etc.) with different morphology and size are being studied through *in vivo* and *vitro* cancer research. Directing anti-cancer agents to tumor cells is perhaps the most demanded topic of nano technological research. Due to leaky and partially permeable blood vessels and poor lymphatic drainage of the tumor sites, nanoparticles can be accumulated in tumors in more doses compared to normal tissues. This passive targeting mechanism is known as enhanced permeation and retention effect (EPR). A study by Li and Huang [35] showed that particles between 100-200 nm size can provide up to four times higher tumor uptake compared to larger or smaller particles [34], [36], [37].

Active targeting, on the other hand, needs more focus on the chemical and molecular differences between cancer and healthy cells. Functionalizing nanoparticles with certain cell receptors,

recognizable only by cancer cells, can minimize toxicity and damage to healthy cells. Accordingly, nanoparticles alone or combined with chemotherapeutical agents encapsulated/attached can be used for selective tumor destruction with minimal damage to normal tissues.

The toxicity of nanoparticles in absence of any therapeutic arise from elevated oxidative stress caused by reactive oxygen species (ROS). ROS can be categorized as two groups: radicals and non-radicals. The former one has unpaired electrons such as superoxide (O2•−) and hydroxyl (HO•) radicals. The latter one does not possess unpaired electron, however, it is chemically active and has the potential to be transformed to radicals, *e.g.*, hydrogen peroxide (H_2O_2). In biological systems they are generated regularly as a natural byproduct and are important in regulating signal transduction pathways. ROS are dynamically regulated through generation and elimination processes to keep oxidative stress at acceptable levels [38], [39].

Because of their metabolic abnormalities in cancer cells oxidant and antioxidant balance cannot be maintained. Thus, they possess higher oxidative stress (or less antioxidant) which makes them defenseless to further oxidative stress by extrinsic agents. This oxygen stress differentiation between malignant and normal cells is employed in cancer therapy.

Since nanoparticles can elevate oxidative stress depending on their surface properties they are good candidates to be used as anti-cancer agents. Nanoparticles' toxic potential is strongly influenced by their size and the shape. In general, smaller particles can generate much more ROS due to their increased surface defects, decreased nano crystal quality, and higher electron donor-acceptor impurities.

A research by Pal *et al.* [40] showed the shape dependent toxicity of silver nanoparticles for inhibition of *Escherichia coli*. In their research, they used truncated triangular nano plates, spherical nanoparticles, and rod-like silver nanoparticles. As the study showed, the nanoparticles in the different shapes, depending on the number of their active facets, represent different inhibition levels from highest to lowest, respectively. Thus, the particles having (111) facets, *i.e.* the most truncated triangular nano plates, favored more inhibition of *E. coli* [40].

2. Experimental

2.1 Materials

The information of all materials and chemicals used in the present study are tabulated in Table 3.

Table 3 Materials used in the present work.

Chemicals	Manufacturer	Purity
Deionized Water	Clean Room Kiel	-
Zinc Acetate	Sigma Aldrich	99.99%
Hydrogen Peroxide Solution	Sigma Aldrich	29-32%
Silver Nitrate	Sigma Aldrich	99%
Isopropanol	Sigma Aldrich	99.5%
Ammonium Hydroxide	Sigma Aldrich	≥95%
Formic Acid	Sigma Aldrich	28-30% in H_2O
Bombyx Mori Silk Cocoons	Shandong Guangtong Home Tex. Co. Ltd.	-
Sea urchin, sea snail, abalone shell	Nadeco	
Sodium Carbonate	Sigma Aldrich	100.00%
Sodium Hydroxide	Sigma Aldrich	≥98 %
Potassium Hydroxide	Sigma Aldrich	90%
Manganese Acetate	Sigma Aldrich	100.00%
Lead Acetate	Sigma Aldrich	100.00%
Copper Acetate	Sigma Aldrich	98%
Cobalt Acetate	Sigma Aldrich	≥98 %
Cadmium Acetate	Sigma Aldrich	≥98 %
Iron Acetate	Sigma Aldrich	95%
Barium Acetate	Sigma Aldrich	98%
Nickel Acetate	Sigma Aldrich	100.00%

2.2 Characterizations

2.2.1 Ultraviolet–visible (UV-Vis) spectroscopy

UV-Vis (Ultraviolet and Visible) spectroscopy measures the transmission or reflection of materials between UV (190 nm) and visible (900 nm) range of the wavelength. Materials to be investigated can be in solid, liquid or gas phase. The technique is mostly used in quantitative and/or qualitative characterization of biological macromolecules, size and concentration of (noble and transition metal) nanoparticles and ions as well as conjugated organic molecules.

UV-Vis spectroscopy is extensively used for the characterization of noble metal nanoparticles since such materials show strong absorption band in visible spectrum due to their localized surface plasmon resonance (LSPR). LSPR occurs when the frequency of the incoming light is resonant with the collective oscillation of the conduction electrons of the nanoparticles.

In a typical UV-Vis spectrometer, the main components are a light source (UV-visible-NIR), a diffraction grating system to dispense the beam of light into single wavelength and a detector to collect the transmitted/reflected intensity of light. In a typical UV-Vis plot, *x*-axis is designated as wavelength/wavenumbers (nm, cm^{-1}) and *y*-axis shows the intensity (mostly in %) for absorption, transmission or reflection modes. The construction schema of the spectrometer can be seen in Figure 5 [41], [42].

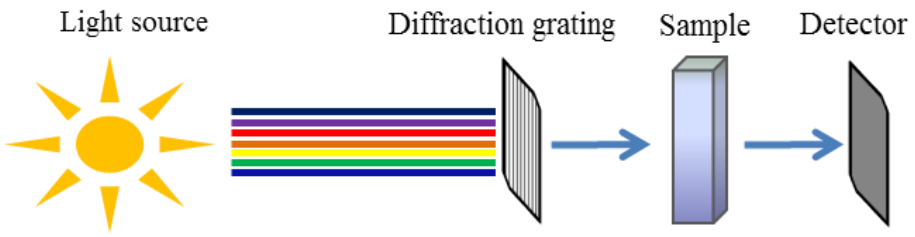

Figure 5 Schematic representation of a UV-Vis spectrometer.

For our measurements, we used UV/VIS/NIR Spectrometer Lambda900 from *Perkin Elmer*. Solution samples were measured in rectangular quartz macro cell cuvettes with two polished sides having either 1 cm path length (3.5 mL volume) or 0.3 cm path length (700 µL volume). The high concentrated samples were diluted with distilled water in given ratios (the dilution ratios are defined in the experimental part). Solid samples were cast on glass slides and measured without any preparation. Calibration measurements were done based on dH_2O and glass slides for solutions and solid samples, respectively.

2.2.2 Fluorescence spectroscopy

The emission of light from any substance is called luminescent. Based on the excited state, the emission is sorted in two subgroups: fluorescence and phosphorescence.

The fluorescence mode corresponds to the singlet excited state where an electron in the excited orbital is paired to the second electron in the ground state orbital. In this case, the emission of the

photon is spin allowed and occurs very rapidly giving rise to typical fluorescence lifetime around 10 ns. [27]

Phosphorescence on the other hand is a triplet excited state. Here, the electron spin orientation of the ground state and excited orbital are the same, preventing transitions to the ground state. Consequently, the emission rate is slower and characteristic phosphorescence life times are between milliseconds to seconds. [27]

In the absorption mode, electrons are excited from the ground state to higher vibrational states. Multiple vibrational states create a blunt peak in an absorption spectrum. Contrarily, the excited molecule is transferred to the lowest vibrational state as a result of vibrational relaxation and internal conversions building the initial point for fluorescence emission being ground state. Fluorescence always takes place at the same excited electronic energy level. For this reason, its spectrum is always shifted (Stokes shift) to a lower energy level than the equivalent absorption spectrum. As a result of this multiple electronic states in the ground state emission spectra occurs as a broad peak [27]. The basic structure of the instrument can be seen in Figure 6.

Mainly fluorescence spectra are shown based on emission spectra which are recorded at a constant excitation wavelength and the emission is scanned as a function of wavelength. Contrarily, for excitation spectrum, the exciting light is scanned as a function of wavelength at a constant emission.

In the present research, fluorescent measurements were done using LS55 Fluorescence Spectrometer from Perkin Elmer. For measurements, quartz macro cell cuvettes with 4 polished sides and 1 cm path length (3.5 mL total volume) have been used. Each measurement was done on 3 mL of sample volume in 1:5 dilutions with dH_2O. In most cases, 3D scans with 600 nm/s scanning speed and 5 nm step size for excitation wavelength were used. The slit size was chosen to be 10 nm for both excitation and emission modes.

For ion detection measurements the same operation parameters were used. However, this time we kept the emission wavelength constant at 403 nm and observed the emission wavelengths at 245 and 312 nm. Solutions of each acetate compound were diluted in de-ionized water and added to silver solution at pH 11 (1:5 diluted in dH_2O) in required amounts to give the designated end concentration.

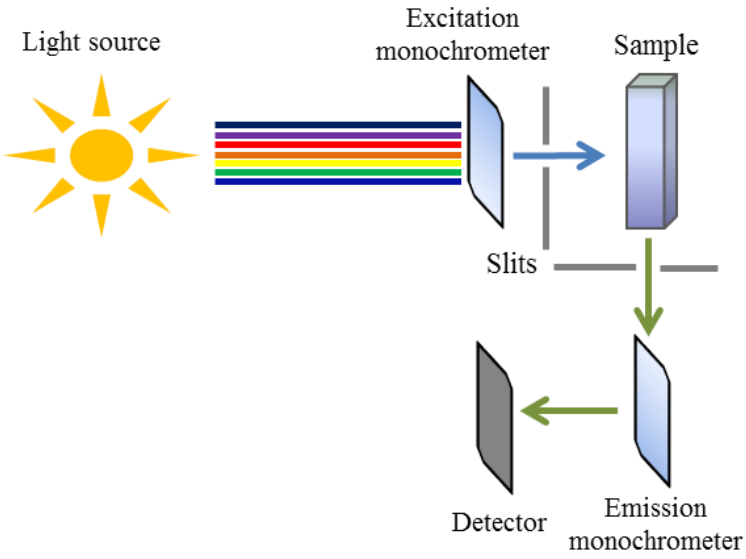

Figure 6 Schematic representation of the fluorescence spectrometer used for emission measurement.

2.2.3 Fourier transform infrared spectroscopy (FTIR)

In this technique, an IR radiation is sent to the sample which then partially absorbed and transmitted. The resulting spectrum characterizes the molecular absorption and transmission, producing a molecular fingerprint of the sample. FTIR is a powerful technique to determine the quality or consistency of a sample or to determine the amount of components in a mixture and identifies chemical bonds in a short period of time [43]. The basic structure of the instrument can be seen in Figure 7.

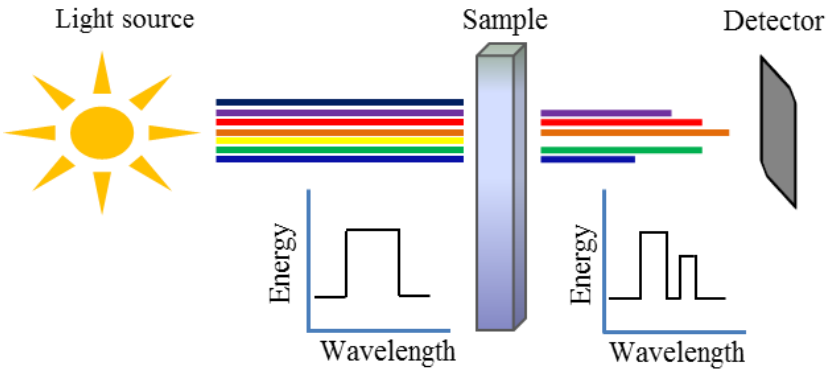

Figure 7 Schematic representation of FTIR.

2.2.4 Scanning electron microscopy (SEM)

SEM is a widely used surface imaging technique in nano technological applications. This technique can offer useful and precise information regarding topography and composition of the sample to be characterized.

In this technique, electrons are ejected from a cathode and focused onto a specimen with the aid of apertures and magnetic (condenser and objective) lenses. The focused beam scans the surface of the specimen through deflection coils. Owing to the interaction of the incident beam and the specimen various signals are made that will be subsequently collected by suitable detectors. Mainly secondary electron and backscattered electron detectors are preferred over Auger and X-ray signals. Secondary electrons have a low escape depth and are used for topographical testing of the sample. Their intensity is dependent on the orientation of the sample with respect to the detector. Backscattered electrons on the other hand are strongly dependent on atomic number of the materials, and are used for comparison of compositional differences or phase changes across the material. Other signals such as X-rays, and Auger electrons are not commonly used in primary sample investigations. A schematic illustration for electron-sample interactions can be seen in Figure 8 [44].

In this study, SEM measurements were carried out using Supra 55VP from *Carl Zeiss Inc*.. The studied samples were prepared either by spin coating or drop casting on silicon substrates. To make the spin coated samples (Spincoater P6700 Series from *Speciality Coating Systems Inc*.) 100 µL of BNC solution were poured on silicon substrates then underwent a spinning with speed of 900 rpm for 80 seconds.

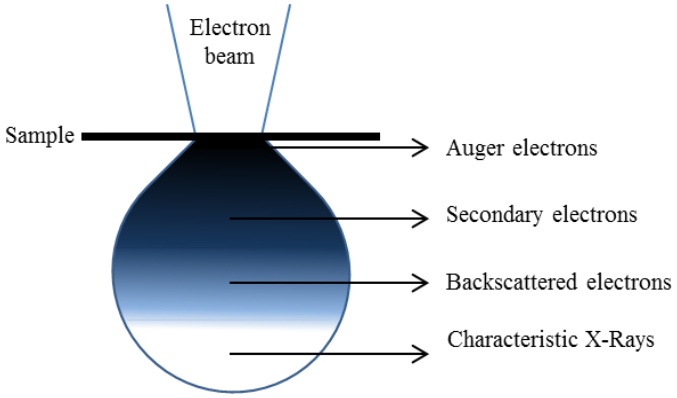

Figure 8 Interaction volumes between the electron beam and the sample.

This step has been repeated three times in order to achieve sufficient amount of nanoparticles for investigation. To make the drop cast samples, depending on the viscosity of the solution single or multiple drops were cast on silicon substrates. The both groups of samples were further dried for sufficient time and if necessary coated with multiple flashes of graphite. For graphite coating Sputter Coater Balzers SCD 050 from *Bal Tec*. has been used.

2.2.5 Transmission electron microscopy (TEM)

TEM uses high energy (100 keV) electrons emitted from an electron gun and accelerated towards samples having thickness of 100 nm or below. The transmitted electrons are magnified through electron optical lenses and form an image on a fluorescent screen. Typical imaging modes are bright field and dark field. In the bright field mode an aperture is used to interrupt scattered/diffracted electrons and contributes to image contrast due to specimen inhomogeneities of density, thickness, and orientation. In the dark field imaging, intensity of diffracted/scattered electrons are used to build up the image and the contrast. Unlike SEM, TEM offers resolutions down to atomic level and provides valuable information about structural properties such as crystal defects, grain size, etc. [44].

In this study, TEM measurements were done using *FEI* Tecnai F30 Stwin G2 from. The samples were prepared by placing a drop of solution on to a copper grid for 30 seconds. The grid was then placed on a deionized water droplet for some seconds and dried at room temperature.

2.2.6 X-ray photoelectron spectroscopy (XPS)

In XPS the sample surface is irradiated with low energy X-rays exciting the electrons with lower binding energies than the X-ray energy. As a result, electrons will be emitted from the parent atom as a photoelectron. Photoelectrons can escape only from the outer most surface between 1-10 nm depths, *i.e.* this method is a surface analysis technique. During their escape from the sample, photoelectrons might be trapped in various excited states or can be subjected to inelastic collisions. Accordingly, stronger signals can be resulted from the components at the surface compared to deeper parts within the detection range of XPS. This feature implies that the technique can be used to estimate the analysis depth in layered materials.

An XPS spectrum is plotted where the *x*-axis describes the binding energy of the electrons and the number of electrons shown on the *y*-axis. Each element shows a characteristic binding energy for

its different electron configurations. The intensity of each peak (number of electrons detected) is proportional to the amount of element in the sampling capacity and can be used further in quantification of atomic percentage values of each element. A typical XPS instrument can be seen in Figure 9 [43], [45].

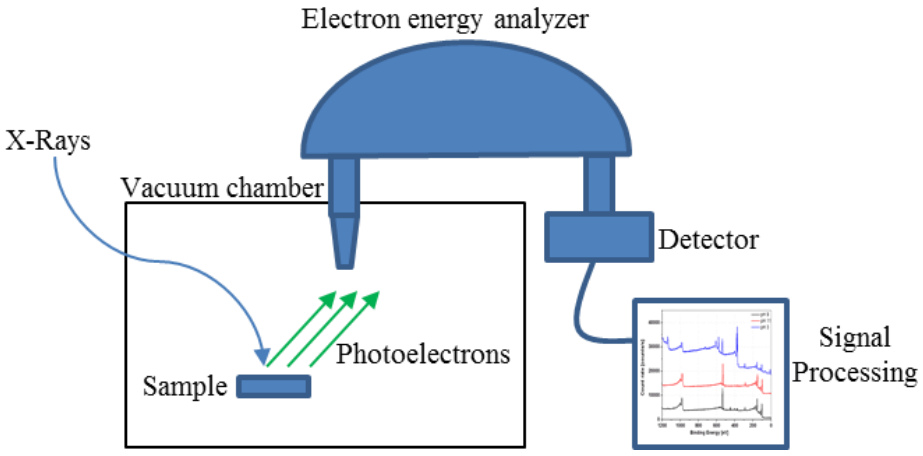

Figure 9 Schematic view of XPS.

XPS measurements were done using Omicron Full Lab with Al source. For sample preparation all the solutions used were washed twice with deionized water (centrifugation at 14000 rpm for 20 min and sonication with deionized water for 10 minutes) in order to have more conclusive signals from the nanocomposites at different pH values. After washing, three layers of each solution (5µL) was spin coated on a silicon substrate.

2.2.7 Atomic force microscopy (AFM)

Atomic force microscopy (AFM) is a tool used to investigate the material topography with aid of a small tip mounted at the free end of a cantilever. During measurements the tip is dragged with constant force along the specimen and repulsive or attractive forces are generated leading to cantilever deflection. The beam deflections are recorded by laser beam reflection from the backside of the cantilever, as shown in Figure 10 [46]. AFM measurements were provided by the Group of Biocompatible Nanomaterials using NanoWizard 3 from *JPK Instruments AG*. The samples were prepared via spin coating (900 rpm, 80 seconds) of a layer of BNC solution of interest (20 µL) onto mica substrates. A schematic illustration of AFM can be seen in Figure 10.

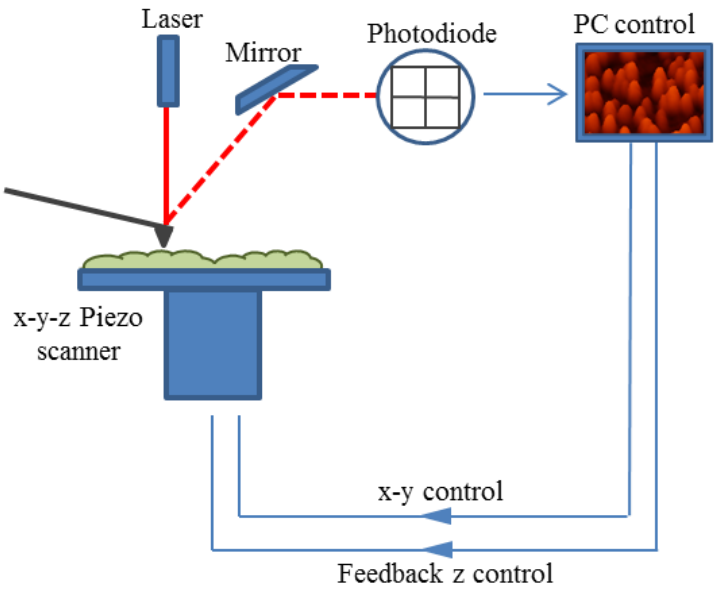

Figure 10 Schematic view of AFM.

2.3 Nanoparticle Synthesis

2.3.1 Silver nanoparticle synthesis

Influence of pH on nanoparticle synthesis

The first synthesis approach is our so called 'one pot synthesis' where bionanocomposites are synthesized simultaneously on the cocoons and within the solution to make colloids. For each experiment 10 mM of $AgNO_3$ (pH 5.5) solution was freshly prepared. To adjust pH, 5 µL of formic acid, 5 µL, or 200 µL ammonium hydroxide were added to 30 mL of silver nitrate solution to achieve the solution at pH values of 3, 9, and 11, respectively. At last, a non-treated cocoon weighing approximately 0.26 g was immersed completely into 30 mL of the pH adjusted solutions. The reference solutions were prepared in absence of $AgNO_3$ salts. In such cases, a non-treated cocoon was immersed into 30 mL of pH adjusted dH_2O. All the solutions were kept at room temperature for several weeks for further investigation. Meanwhile regular measurements were performed by using fluorescence and UV-Vis spectroscopy. Additionally, the dried cocoons of the reference solutions (pH 3, pH 11, and non-modified pH ones) were investigated using fluorescence spectroscopy. For morphological investigations SEM, TEM and in some cases AFM were used. Furthermore, elemental composition of the particles was analyzed using XPS. The experiments for the 'one pot synthesis' of silver nanoparticles can be seen in Table 4 briefly.

As an alternative method to the 'one pot synthesis', synthesis of nanoparticles employing released sericin residues in absence of cocoons was investigated. In this case, the sericin solute was prepared by immersing 20 cocoons (approx. 5.78 g) into 500 mL (a cocoon for each 25 mL) dH_2O and stored at room temperature for three days. Afterwards all the cocoons were removed from the flask and the sericin-solute was directly used without further treatment.

Further experiments were done in order to examine the influence of concentration, and soaking time on sericin release and mixing ratio of silver salts and sericin solute.

To investigate the concentration of sericin on nanoparticle production, the sericin solute was prepared as explained in the previous paragraph. Then, silver nitrate solution was added to solutes in different ratios of 1:1, 1:2 and 1:4 to make 1 or 10 mM $AgNO_3$ concentration in 50 mL of the mixed solution. All the samples were stored at room temperature and UV-Vis absorption measurements were done after 20 minutes, 1, 2, 4 and 5 hours. The experiments for this synthesis through sericin solute can be seen in Table 5.

In order to investigate the effect of temperature and the soaking time on the synthesis, a single cocoon was soaked in 25 mL deionized water for different periods of time either at room temperature or at 50°C (Exp. 15 and 16, respectively). Afterwards, the cocoons were removed and the remaining sericin solute was blended with 2 mM of $AgNO_3$ in 1:1 ratio to reach 1 mM end concentration at room temperature and at 50^oC (Exp. 17 and 18, respectively). UV-Vis measurements were done before the addition of silver nitrate and regularly at each 30 minutes up to 6 hours followed by 24, 48, and 72 hours after addition of silver salt. The experiments can be seen briefly in Table 6.

Temperature and concentration influence on nanoparticle synthesis at pH 3

As stated previously in the introduction, the synthesis at acidic conditions showed interesting adherence behaviors with 10 mM $AgNO_3$ systems. In order to increase the thickness of the coating the influence of different environmental conditions such as temperature and metal salt concentration were investigated. In these investigations, the molarity of silver nitrate was doubled and synthesis was performed at room temperature and at 50°C with identical pH correction. Furthermore, higher concentrations of the samples including 50 mM, 0.25 M, and at 0.5 M $AgNO_3$

at 50°C were observed to explore their influence on film thickness and conductivity. The experiments for this section can be seen in Table 7.

2.3.2 Gold nanoparticle synthesis

The experiments for gold nanoparticles can be seen in Table 8. For each experiment, 1 mM or 0.1 mM of $HAuCl_4$ solution were prepared. Isopropanol was added to the solutions to enhance the reduction potential. To adjust pH, sodium hydroxide or formic acid were added to 30 mL of $HAuCl_4$ solution. At last, a non-treated cocoon weighing approximately 0.26 g was immersed completely into 30 mL of the pH adjusted solutions. The solutions were either kept at room temperature or placed onto a hot plate at 50°C or 100°C. At the end of the experiments UV-Vis measurement was performed.

Table 4 Experiments for silver BNC synthesis with one pot bioshell concept at different pH values.

Experiment #	$AgNO_3$ (mM)	pH	Added buffer	Temperature	Duration
Exp. 1	10	3	5 µL HCOOH	~24ºC (RT)	4 weeks
Exp. 2	10	5.5	-	~24ºC (RT)	4 weeks
Exp. 3	10	9	5 µL NH_4OH	~24ºC (RT)	4 weeks
Exp. 4	10	11	200 µL NH_4OH	~24ºC (RT)	4 weeks
Exp. 5	-	3	~5 µL HCOOH	~24ºC (RT)	4 weeks
Exp. 6	-	7	-	~24ºC (RT)	4 weeks
Exp. 7	-	9	~5 µL NH_4OH	~24ºC (RT)	4 weeks
Exp. 8	-	11	~200 µL NH_4OH	~24ºC (RT)	4 weeks

Table 5 Experiments for silver BNC synthesis with sericin solute concept at different precursor concentration and varying $AgNO_3$:Sericin ratio.

Experiment #	$AgNO_3$ (mM)	$AgNO_3$: Sericin	Temperature	Duration
Exp. 9	1	1:1	~24ºC (RT)	5 Hours
Exp. 10	1	1:2	~24ºC (RT)	5 Hours
Exp. 11	1	1:4	~24ºC (RT)	5 Hours
Exp. 12	10	1:1	~24ºC (RT)	5 Hours
Exp. 13	10	1:2	~24ºC (RT)	5 Hours
Exp. 14	10	1:4	~24ºC (RT)	5 Hours

Table 6 Experiments for sericin release and their contribution to nanoparticle synthesis at different temperatures.

Experiment #	$AgNO_3$ (mM)	Cocoon soaking time	Temperature
Exp. 15 a	-	15 min	~24ºC (RT)
b		30 min	
c		45 min	
d		1 hour	
e		1.5 hours	
f		2 hours	
g		3 hours	
h		6 hours	
i		24 hours	
j		48 hours	
k		72 hours	
Exp. 16 a	-	15 min	50ºC
b		30 min	
c		45 min	
d		1 hour	
e		1.5 hours	
f		2 hours	
g		3 hours	
h		6 hours	
i		24 hours	
j		48 hours	
k		72 hours	
Exp. 17 a	1	15 min	~24ºC (RT)
b		30 min	
c		45 min	
d		1 hour	
e		1.5 hours	
f		2 hours	
g		3 hours	
h		6 hours	
i		24 hours	
j		48 hours	
k		72 hours	
Exp. 18 a	1	15 min	50ºC (RT)
b		30 min	
c		45 min	
d		1 hour	
e		1.5 hours	
f		2 hours	
g		3 hours	
h		6 hours	
i		24 hours	
j		48 hours	
k		72 hours	

Table 7 Experiments for silver BNC synthesis at acidic pH with one pot bioshell concept at different precursor concentration.

Experiment #	$AgNO_3$ (mM)	pH	Temperature
Exp. 19	20	3	~24ºC (RT)
Exp. 20	20	3	50ºC
Exp. 21	50	3	50ºC
Exp. 22	250	3	50ºC
Exp. 23	500	3	50ºC

Table 8 Experiments for gold BNC synthesis with one pot bioshell concept at different pH values and temperatures.

Experiment #	$HAuCl_4$ (mM)	pH	Temperature	C_3H_8O
Exp. 24	0.1	3.5	50ºC	-
Exp. 25	0.1	2.7	50ºC	-
Exp. 26	0.1	2.7	100ºC	-
Exp. 27	1	3.4	~24ºC (RT)	-
Exp. 28	1	7.5	~24ºC (RT)	-
Exp. 29	1	3.4	50ºC	-
Exp. 30	1	3.4	50ºC	500 µL

3. Results and Discussion

3.1 Silver bionanocomposites made through the Bioshell concept

Our concept is basically a green, cost effective, and versatile technique which uses natural substances to produce silver and gold bionanocomposites. We call it simply "bioshell technique' because the natural materials we use are a nourishing or protecting shell/house/shelter for diverse animals. Since these materials are the nourishing and protecting part of the animals, they are rich in proteins, lipids, vitamins and enzymes, *i.e.* supplying the necessary environment for synthesizing metal bionanocomposites. The biomolecules present in the shells are diverse in terms of hydrophobicity and acidity. This variety enables their activation through different environmental parameters such as acidic-basic pH, or temperature. Accordingly, the synthesis can be tailored depending on the end product's requirements.

Some examples to our bioshells include cocoons of mulberry silk worm, sea urchins, abalones, sea snails, and starfish (Figure 11). Thanks to flexibility and compressibility, cocoons can be introduced as soft bioshells, while the rest will be referred as hard bioshell owing to their rigidness. In the present work we focused mainly on the synthesis of bionanocomposites through soft bioshells. However, preliminary research regarding the synthesis of bionanocomposites through hard bioshells such as sea urchins will be shown briefly.

In both cases the applicable concept and the basic synthesis procedure are shown in Figure 12. But the procedure of soft bioshells is the main focus of the present study. Here, a bioshell is shown as a sphere whose inner and outer sides are decorated with hydrophilic/phobic biomolecules, Figure 12a. When the bioshell is immersed into a salt solution (Figure 12b), the metal ions are located at the hydrophilic and phobic sites. Subsequently, (Figure 12c) the hydrophilic sections are gradually detached into the salt solution while interacting with metal ions. Ultimately, (Figure 12d) on both sections (hydrophilic and phobic) of the bioshell, nanoparticles are formed and accumulate, creating nanoclusters.

The amount and the type of biomolecules released from the bioshell can be selectively adjusted by changing temperature and pH. Different environmental conditions result in release of biomolecules in diverse sizes, yield, filling factor, and structure. These structural variations can be easily tracked by the changes of the plasmonic properties of the formed bionanocomposites.

A wide range of bionanocomposites produced through our concept can be seen in Figure 13 and Figure 14. In Figure 13 we see hard bioshells covered with silver BNCs. Figure 13g and Figure 13h show SEM image of a sea urchin decorated with silver nanoparticles. The synthesis is so effective that even a porous and complicated structure can be evenly decorated with nanoparticles. For comparison, the SEM image of a bare urchin is shown in Figure 13i. The released biomolecules from sea urchin produce silver nanoparticles having brown plasmonic color within the solution and on the urchin body simultaneously (Figure 13j). Figure 14 shows the synthesis of bionanocomposites through soft bioshells. In this figure the bioshells and their corresponding colloids having miscellaneous plasmonic colors.

The idea of using biomolecules to synthesize nanoparticles is not novel, however, our approach shows a more effective way to synthesize the nanoparticles. Unlike the studies reported previously, in this work a complicated extraction method was simplified and cocoons were used as received. Accordingly, we were able to benefit from full potential of all the bio substances and create many additional properties such as adhesiveness which were not shown previously with similar methods based on my knowledge.

3.2 Soft bioshells and bionanocomposites synthesis

Sericin, a sticky protein enveloping the twin threaded fibroin fibrils, is the key protein in our research. It can readily be dissolved in water due to its hydrophilic nature. Once it is removed only loose tiny threads of fibroins remain. The SEM image of these fibers are shown in Figure 15.

In this study the synthesis of BNCs via cocoons at different experimental parameters such as pH, temperature and concentration of silver salts is investigated. Among these parameters, the influence of pH was highlighted and the pH of the solutions were adjusted at four values of pH 3 (Exp. 1), pH 5.5 (Exp. 2), pH 9 (Exp. 3), and pH 11 (Exp. 4). From now on pH 3 condition will be referred as acidic, and pH 9 and pH 11 will be referred as alkaline conditions.

Figure 11 Examples of soft and hard bioshells used in our study.

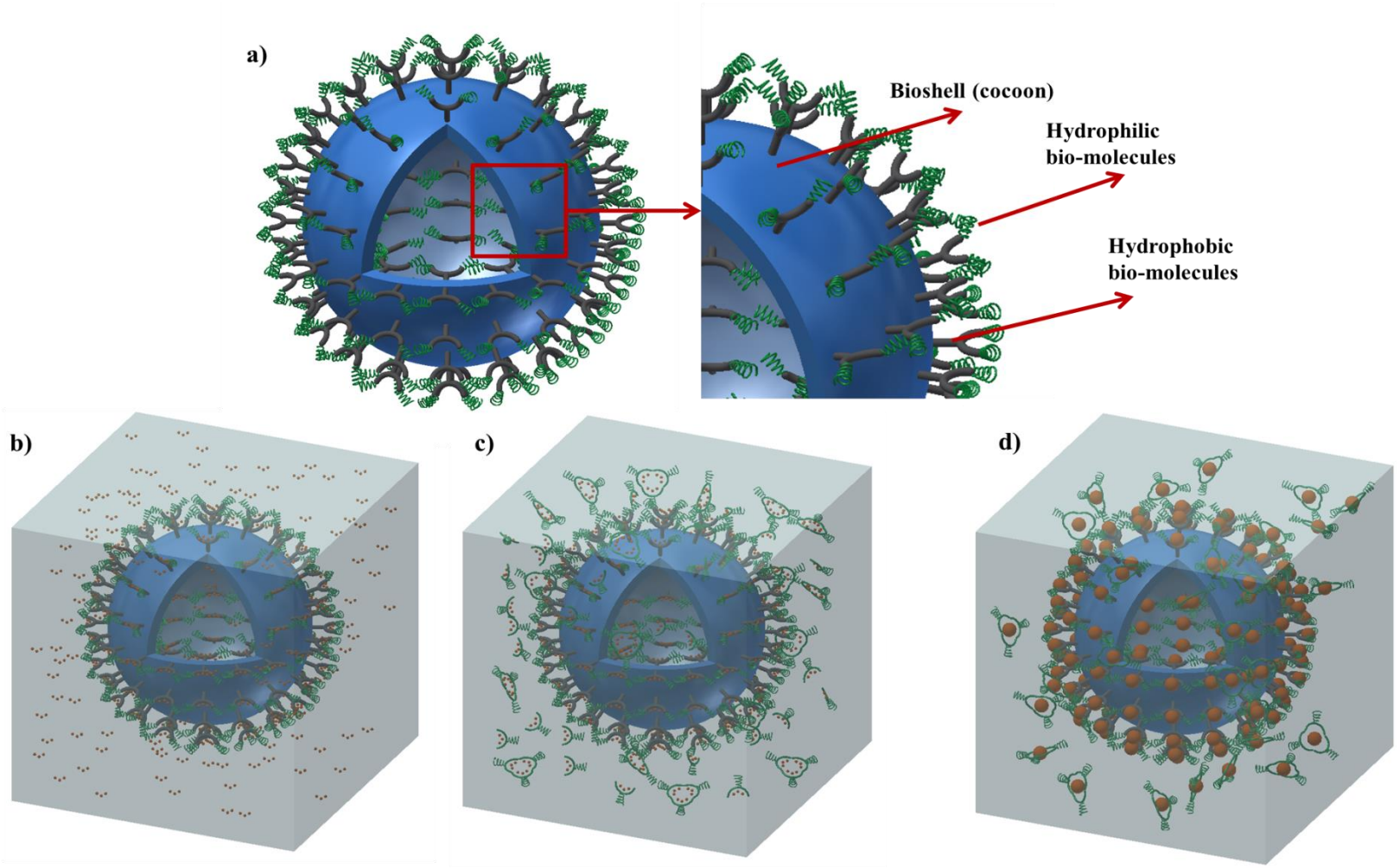

Figure 12 Schematic illustration of the bioshell concept. a) The shell covered with hydrophilic-phobic molecules. b) Bioshell immersed into salt solution and released ions are attracted to both hydrophilic and hydrophobic parts of the bioshell. c) Due to a reduction process the first nanoparticle formation starts. d) Allowing necessary reaction time the nanoparticles grow forming bionanocomposites, *i.e.* metallic nanoparticles encapsulated with biomolecules.

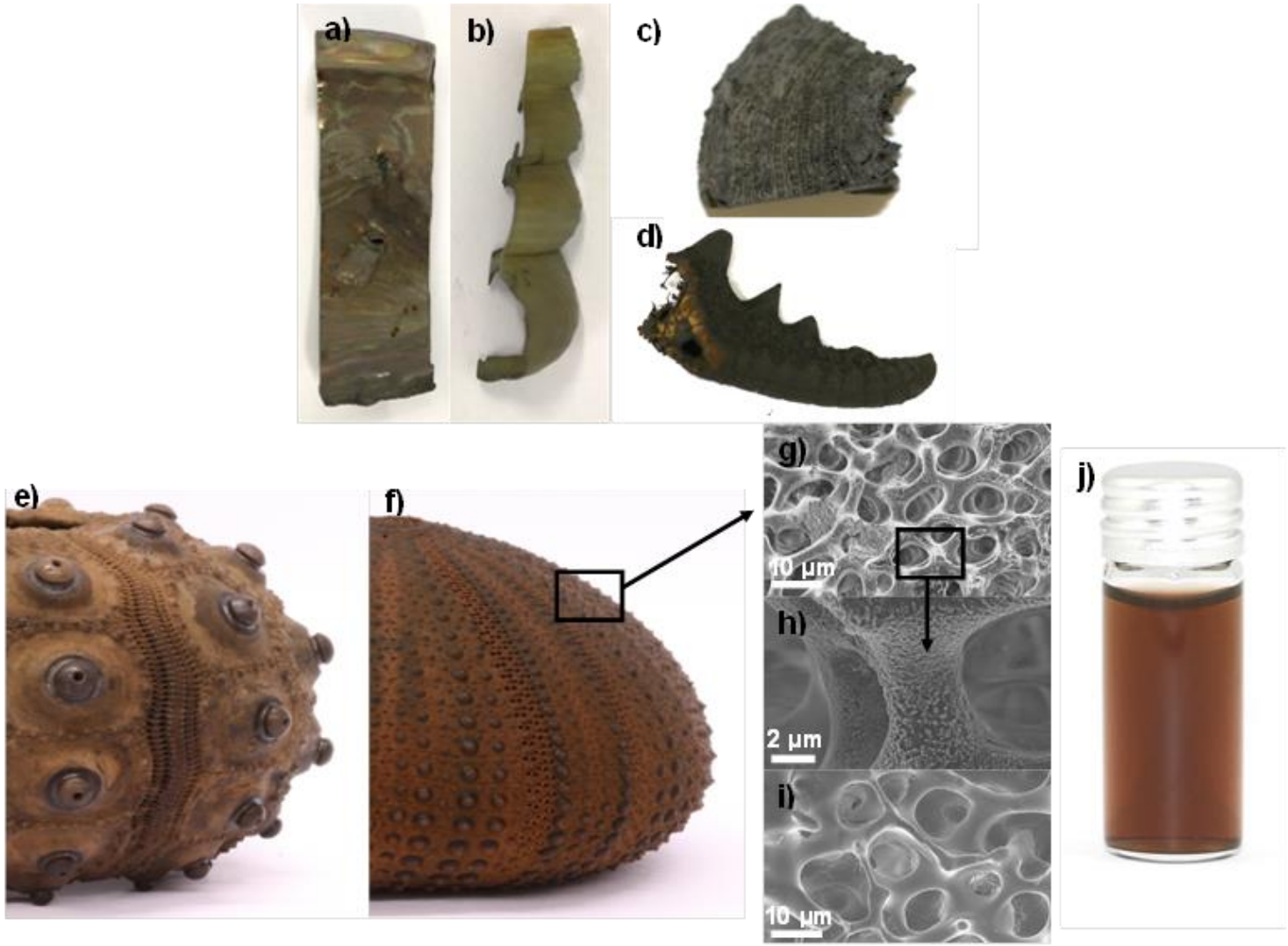

Figure 13 Hard bioshells after synthesis. The brownish colour comes from the silver nanoparticles attached. a) Abalone b) and c) sea snail, d) star fish e) sea urchin f) green sea urchin g) and h) SEM images of a sea urchin after synthesis with silver nitrate i) SEM image of a bare urchin before synthesis j) a colloidal solution with brown plasmonic color.

Figure 14 Colloidal solutions and the relevant soft bioshells decorated with silver and gold nanoparticles thereby shining in miscellaneous plasmonic colors.

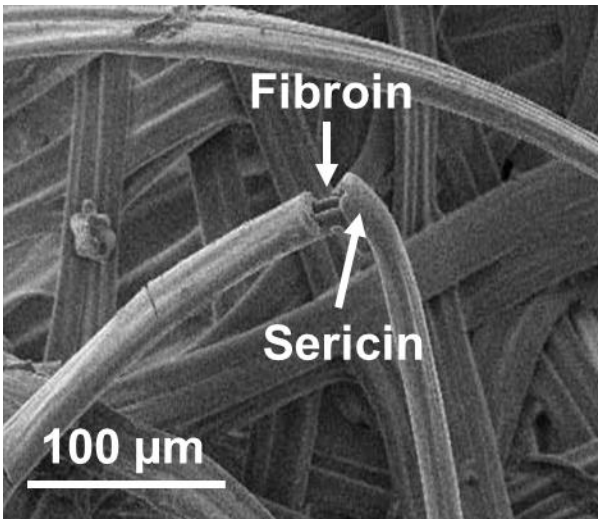

Figure 15 SEM image of cocoon threads containing twinned fibroin fibrils enveloped in sericin.

Upon immersion of cocoons in water, the dissolution of sericin starts. This effect can be observed by naked eye due to mild turbidity of the water. Moreover, SEM and UV-Vis spectrometry can also verify this behavior as shown in Figure 16. In Figure 16a the SEM images reveal the dissolution of the biomolecules as spherical colloidals. Additionally, plasmonic bands appearing at 275 nm attributed to aromatic amino acids imply the dissolution of sericin (Figure 16b). As the pH of the solution changes different portions and-or different conformations of the sericin is expected to be dissolved into solution. These changes can be tracked by FTIR and fluorescence spectroscopy. FTIR is a key tool in order to investigate secondary structures of amino acids and their modifications. There are nine IR absorptions bands which are A, B, and I-VII. Among those Amide I and Amide II bands are the most important ones due to the amount of information. Figure 17 shows the FTIR spectrum of the sericin release of Exp. 5, 7 and 8.

The peaks between 900 and 1200 cm^{-1} can be assigned to different amino acid residues. The most obvious ones being around 980, 1040, 1065, 1115 cm^{-1} can be assigned to Ser, ν(CO) or ν(CC), Ser, ν(C-O), Trp, ν(NC), δ(CH), ν(CC), His, ν(CN), δ(CH), respectively. Among these peaks, both sericin peaks show the highest intensity for Exp. 8 (pH 11). The peaks related to Tryptophan and histidine are very weak for Exp. 5 and Exp. 7 (pH 3 and 9), respectively. The peaks between 1220 and 1301 cm^{-1}, attributed to Amide III region, seem to be similar for Exp. 5 and Exp. 8 [47], [48].

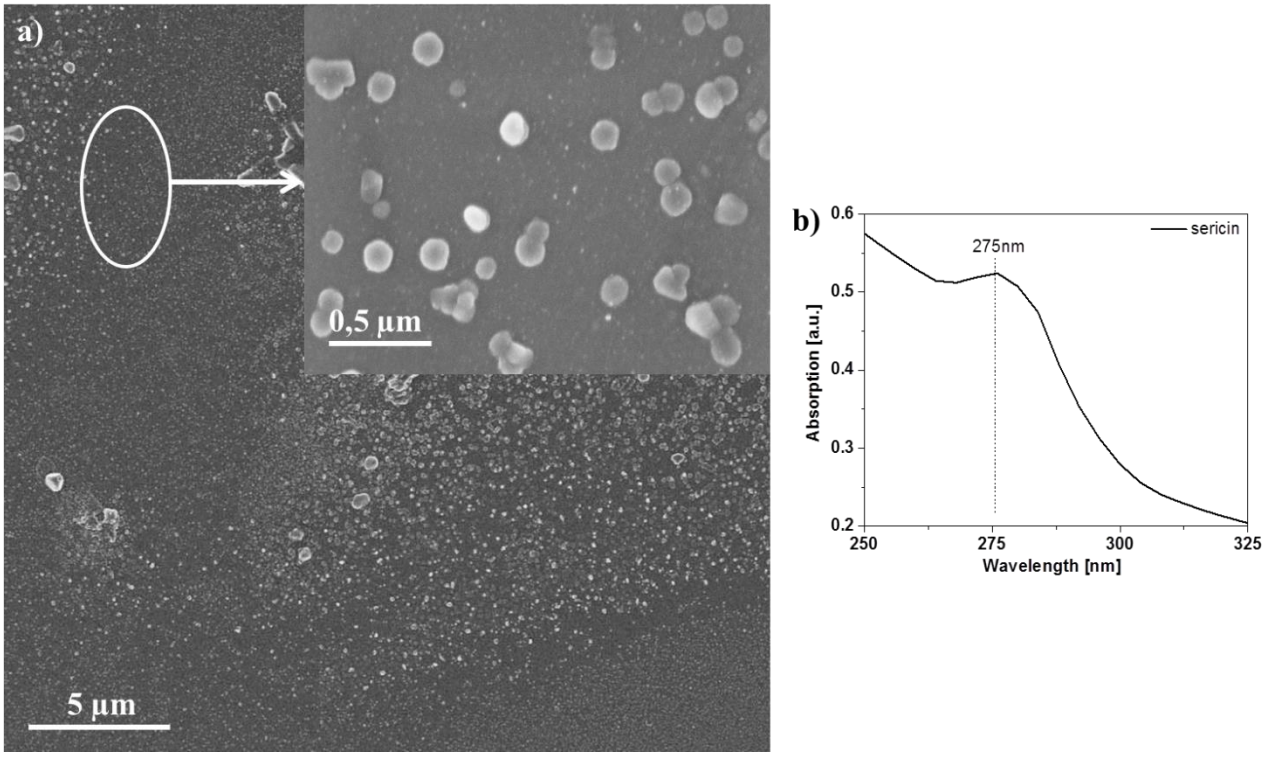

Figure 16 a) SEM image verifying sericin release as a dense area full of bio residues at nanoscale b) UV/Vis absorption spectrum of sericin release revealing a peak at 275 nm.

Another prominent peak around 1380 cm^{-1} can be assigned to δs(CH3). For Exp. 7, the peak is displaced to higher wavenumbers. Afterwards, the Amide II region between 1480-1575 cm^{-1} varies significantly for each sample. Amide II vibration arises mainly from in-plane NH and CN stretching vibrations. For Exp. 5, it is observed at 1576 cm^{-1}, *i.e.* the region of beta fold structure. For Exp. 7, it is located at 1545 cm^{-1} implying random coil structure of sericin. For Exp. 8, coexistence of beta fold and random coil was detected. For Exp. 8 the region between 1500 and 1626 cm^{-1} is composed of many small peaks. A faint shoulder at 1510 cm^{-1} and a small peak at 1539 cm^{-1} can be assigned to beta fold and random coil structures, respectively. Amide I arising from C=O stretching vibrations is observed between 1600-1700 cm^{-1}.

Secondary structures are constructed with characteristic pattern of hydrogen bonding between C=O and N-H groups: due to that fact Individual secondary structures for typical amide absorptions are expected. The strength of the hydrogen bond linked to amide C=O group determines the band position. A stronger hydrogen bond lowers the electron density and the Amide I absorption. Amide I band for Exp. 8 is observed around 1626 cm^{-1} as a small peak and for Exp. 5 and 7 appears only as a shoulder [48], [49], [50].

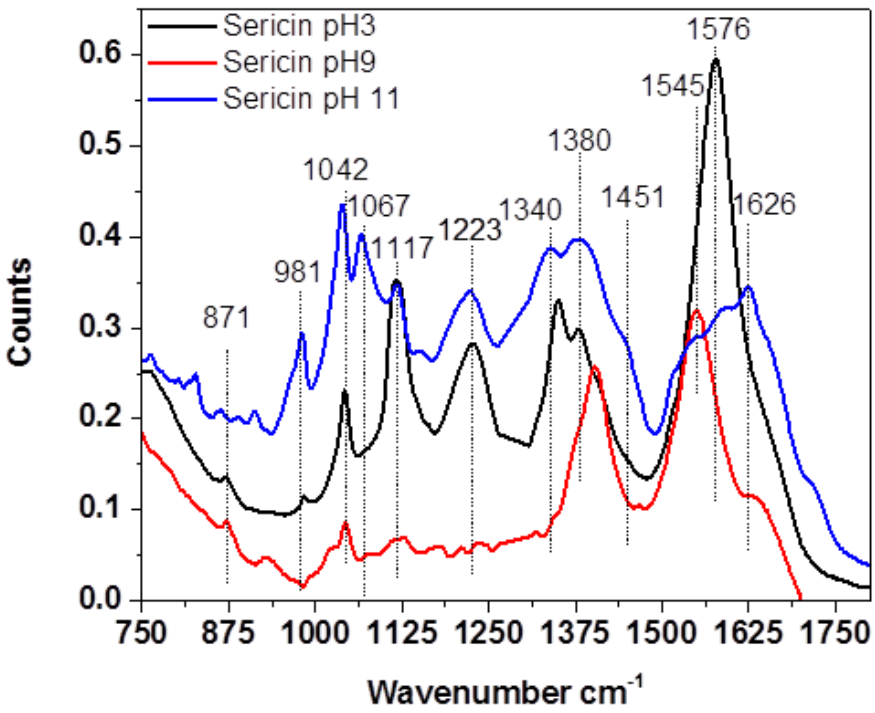

Figure 17 FTIR plot of sericin releases for Exp. 5 (pH 3), Exp. 7 (pH 9) and Exp. 8 (pH 11).

Based on FTIR results, it is obvious that pH influences the conformation of the sericin residues released. The comparison of FTIR bands after BNC synthesis which will appear in the following pages will help us to understand the role of different protein residues better.

The sericin released could be also detected by using fluorescence spectroscopy. Figure 18 shows the contour maps obtained through fluorescence spectroscopy for the sericin released at given pH values. A simple glimpse on the images can readily reveal the pH induced changes.

In contour maps shown in Figure 18 the emission wavelength of 300-365 nm with 275 nm excitation is attributed to Tyr or Trp residues [51]. The intensity of this peak declines in the order from Exp. 8, Exp. 5 to Exp. 7. Another peak appearing at 400 nm emission wavelength with 312 and/or 245 nm excitation is attributed to dityrosine and can be seen at all pH values [52]. In addition to amino acids, enzymes such as NADH and Pyridoxal are also observed in the contour maps around 425 nm and 375 nm emissions, respectively. NADH is prominent for Exp. 7 (pH 9) and Exp. 5 (pH 3); however, it is absent in Exp. 8 (pH 11). Moreover, Pyridoxal is observed only at pH 3. The presence of different biomolecules due to environmental variations such as pH changes strongly affects the synthesis. In the first experiments, 10 mM $AgNO_3$ was used at pH values mentioned previously within a four-week course (Exp. 1-4). Interestingly, pH variation led

to creation of a diverse range of plasmonic colors (see Figure 19). The synthesis at the highest pH (Exp. 4) resulted in formation of a yellowish plasmonic color that was stable throughout the four weeks. Absorption peak of the solution was noted at 440 nm (Figure 20). The respective cocoon's color on the other hand changed from pale yellow to brown within the same time range.

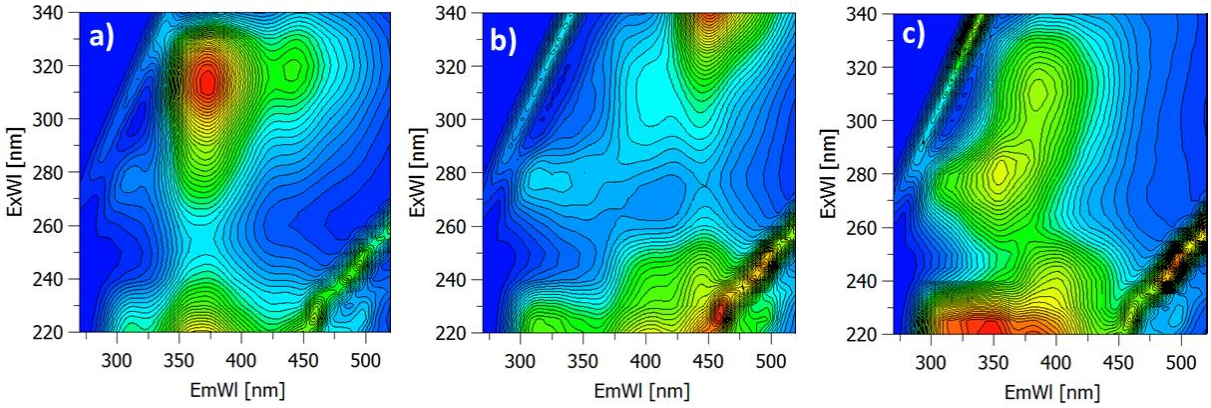

Figure 18 Fluorescence Spectroscopy contour maps of the sericin released for a) Exp. 5 (pH 3) b) Exp. 7 (pH 9) and c) Exp. 8 (pH 11).

Figure 19 Colloidal solutions of the bionanocomposites and cocoons inside decorated with nanoparticles. Due to high intensity the solution with pH 3 was diluted 1:2 with dH_2O.

When the alkalinity dropped to pH 9 (Exp. 3), a yellow brownish colloid was made which became reddish with time with a corresponding plasmon peak around 450 nm (Figure 20). Its cocoon was brownish, indicating high amount of nanoparticles generated on the fibers. The reason for the high

yield of nanocomposites on the cocoon as well as in the solution is explained in the upcoming pages.

At pH 5.5 (Exp. 2), the original pH value of 10 mM $AgNO_3$, a very pale yellowish solution with a very small intensity in UV-Vis spectrum was created (Figure 20): its cocoon on the other hand had a pale orange to brownish hue. The most promising and interesting results were observed at pH 3 (Exp. 1). Here, the yield increased significantly and different absorption spectra having two peaks located around 410 nm and 610 nm were recorded. The yield for Exp. 1 was relatively high compared to samples obtained at other pH values. Due to their high concentration UV-Vis absorption measurement for Exp. 1 were performed by dilution of distilled water in order to get reasonable signals.

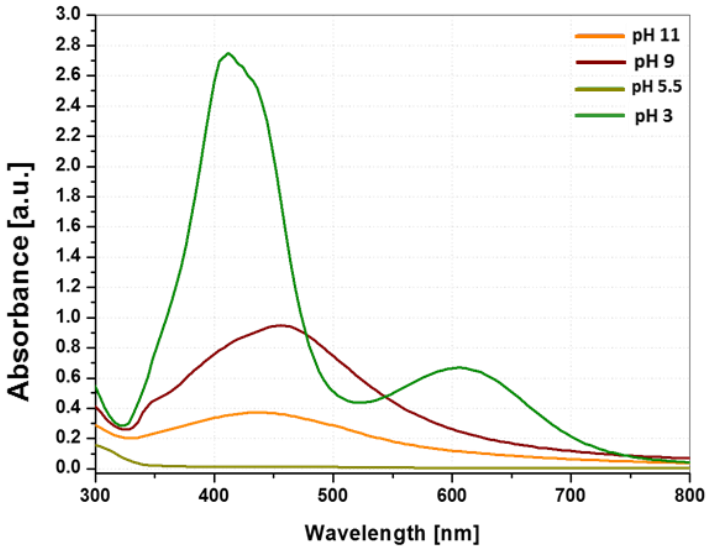

Figure 20 UV-Vis spectra of the bionanocomposites for Exp. 1-4.

In order to compare the yield as well as to get a bit more information about the surface composition, XPS measurements were also performed. The results are demonstrated in Figure 21.

XPS spectra of the bionanocomposites solution show distinctive peaks for Ag 3d/3p. The peak intensity is at its highest level for Exp. 1 whereas it is at moderate and the lowest level for Exp. 3 and Exp. 4, respectively. Since the counts are directly related to elemental compositions, as our experiments suggest the Ag yield is highest for Exp. 1 and lowest for Exp. 4 synthesis. Except the Ag peaks, the N counts showed slight increase for Exp. 1. At last, a small shift in C 1s was also observed.

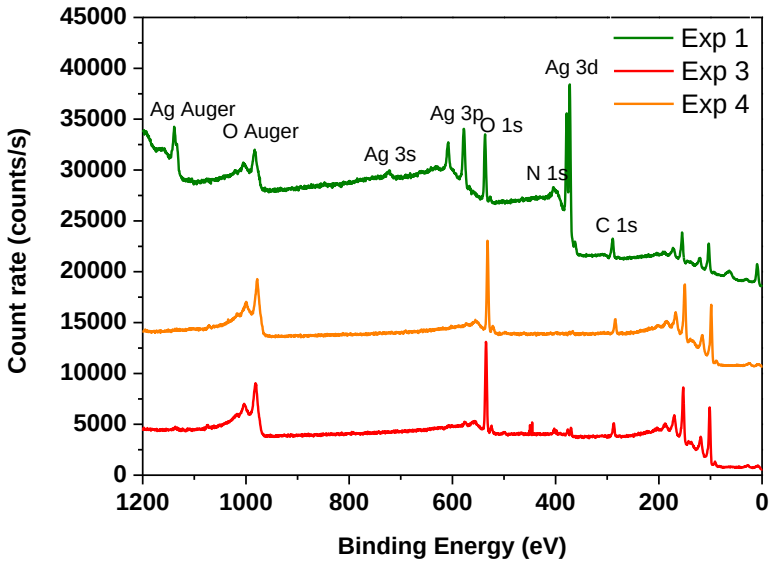

Figure 21 XPS spectra of the solutions of Exp. 1 (pH 3), Exp. 3 (pH 9) and Exp. 4 (pH 11) colloidals.

In order to have an understanding to BNC formation through biomolecules, in the following, FTIR and Fluorescence spectroscopy results after synthesis will be presented.

As shown in FTIR spectra (Figure 22) the peaks between 900 and 1200 cm^{-1} appear also for the BNC synthesis however as slightly shifted (except for Exp. 1). Moreover, for Exp. 1 the intensity of the relevant peaks drops drastically for all the bands of Ser, Trp and His. This indicates that the residues mentioned are mainly involved in the pH 3 BCN synthesis.

In the amide III region, *i.e.* between 1229 and 1301 cm^{-1}, a peak around 1300 cm^{-1} (1301 cm^{-1} for pH 3 and 1312 cm^{-1} for pH 9) appears for all nanoparticle syntheses that can be attributed to C-H bending of aromatic groups [53]. Due to some errors in the analysis of the pH 11 sample, the 1300 cm^{-1} peak was off the scale and smoothed. Because of that, the exact location of the band cannot be found; however, the increasing trend of this peak at the same area proves the similar behavior as the samples synthesized at other pH values. Another band which can be attributed to aromatic vibrations is found at much lower wavenumber around 810 cm^{-1}. Specifically, this peak is attributed to C (aromatic)-H in-plane bending vibrations. Both peaks related to aromatic vibrations exist only at nanoparticles conjugated with sericin and not in sericin release solely, implying the role of aromatic residues in the synthesis. As mentioned previously, aromatic amino acids can

donate an electron to metal cations to form metal nanoparticles which is also confirmed through this FTIR analysis [47], [48].

Another prominent peak appearing around 1370 cm^{-1} can be assigned to δs(CH3). The location of this peak is same for basic conditions; however, it shifts slightly for Exp. 1. In another region, the Amide II region, the peak observed at 1575 cm^{-1} for Exp. 1 for beta fold structure disappears during the nanoparticle synthesis. For Exp. 3 the sericin release peak at 1550 cm^{-1}, implying random coil structure, is converted to beta fold structure during nanoparticle synthesis and appear at 1526 cm^{1}.

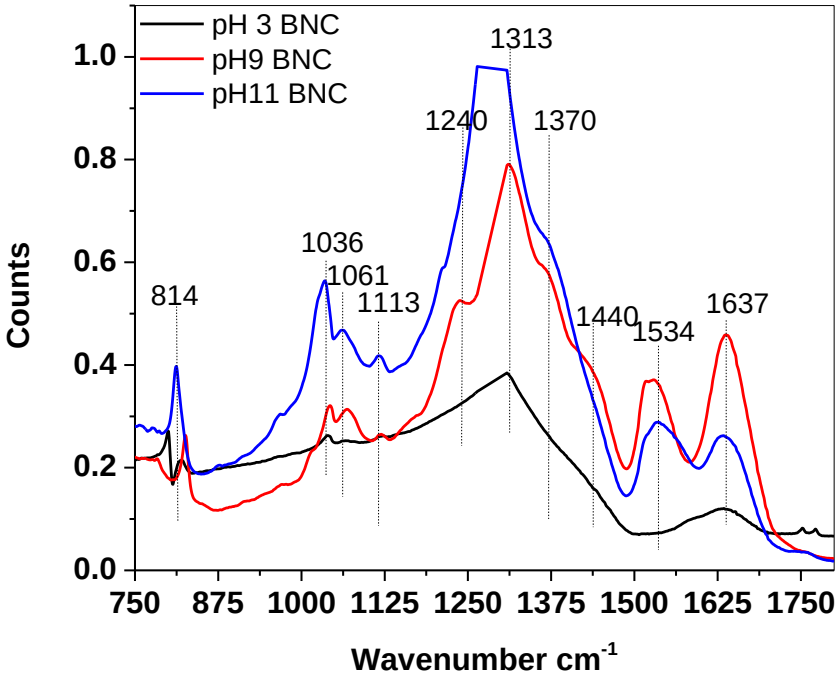

Figure 22 FTIR spectra for the BNC synthesis at Exp. 1 (pH 3), Exp. 3 (pH 9) and Exp. 4 (pH 11).

For Exp. 4, beta fold and random coil co-exist and during the nanoparticle synthesis, the peak at 1539 cm^{-1} becomes prominent with a shoulder at 1510 cm^{-1}. Amide I arises from C=O stretching vibrations and is observed between 1600-1700 cm^{-1}. The peaks observed previously for the sericin release is intensified during synthesis [48], [49], [50].

If we continue with the fluorescence results, we also see the contribution of amino acids in to nanoparticle synthesis clearly. Figure 23 shows the contour maps for the BNCs synthesis.

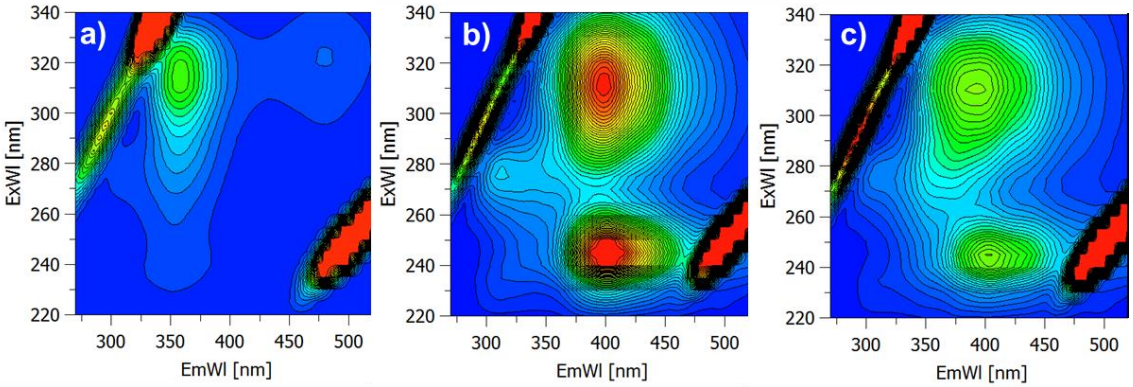

Figure 23 Fluorescence spectroscopy for the BNC synthesis for a) Exp. 1 (pH 3) b) Exp. 3 (pH 9) and c) Exp. 4 (pH 11).

For Exp. 4 (pH 11), the dominant peaks of Tyr and Trp are vanished during the synthesis and dityrosine was observed in both of the solutions. The possible reduction mechanism could be as follow: tyrosine is ionized to tyrosinate and reduces the metal ion forming tyrosil radicals. Two tyrosil radicals are linked and make dityrosine bridge increasing the intensity of dityrosine peak in the fluorescence maps.

BNC solutions of Exp. 3 and Exp. 4 are quite similar especially regarding the dominant peak of dityrosine. Thus, in the reference solution other than the Tyr and Trp peaks an additional peak of NADH was observed which was absent in the nanoparticle solution. NADH is an enzyme with no reducing capability on its own, however, it can act as a catalyst [54]. It also does not show fluorescence in its oxidized form. Thus, its absence suggests that it is either used or oxidized during synthesis.

To summarize, metal ions are reduced to metals by tyrosine residues. NADH, on the other hand, acts as a catalyzer and increases the synthesis yield. This theory complies with the higher absorption intensity of the Exp. 3 colloidals with its red color compared to Exp. 4.

Exp. 5 (reference solution at pH 3) shows the peaks of Tyr, and Trp residues, additionally the peaks related to Pyridoxal and NADH appear at 375 nm emission and 425 nm emissions, respectively. During the synthesis, all these peaks are vanished and unlike alkaline solutions no peak for dityrosine is observed. Consequently, it is assumed that the reducing mechanism is actualized through consumption or oxidation of Pyridoxal and accelerated via NADH residues.

As it turned out, the differences in the synthesis yield and its kinetics can be explained through the different reduction paths triggered by pH. The biogenic synthesis is accomplished by amino acids (Tyr, Trp) and the released enzymes (NADH, Pyridoxal) at alkaline and acidic environment, respectively.

NADH and Pyridoxal are important enzymes to protect and nourish cocoon. Pyridoxal and Tyr which are both rich in hydroxyphenylalanine groups provide cocoon (sericin) with its sticky nature. Despite the existence of Tyr/Trp peak in the reference solutions, Pyridoxal signal was recorded only in the acidic conditions.

Above their isoelectric point, amino acids and enzymes are oxidized and lose their characteristics. At low acidity, on the other hand, they exist in their native form and keep their characteristics such as adhesiveness (in the case of Pyridoxal) and reducing capability (in the case of Tyr), bringing about high yields. Thus, only at acidic environment conditions both promising features are observed.

Further fluorescence measurements (Figure 24) showed that fluorescence peaks obtained from the cocoons of Exp. 6 and Exp. 5 are common in the solution containing nanoparticle and reference solutions. This indicates that the released biomolecules at acidic conditions (Exp. 5) are the same as the ones on pure cocoon surface. Since the cocoon itself is covered by adhesive protein of sericin, the findings mentioned previously are in consistency.

Since in all similar researches to this one, sericin has been used after long treatments, the adhesive residues of sericin as well as Tyr and Trp groups have been most probably partially or totally oxidized, and denatured. Our “One pot” synthesis used in the present study succeeded to overcome this challenge and resulted in a high yield synthesis of multifunctional nanocomposites. Colloids of Exp. 1 show core-shell nanoparticles with a size around 40 nm, while for the sample of Exp. 3, particles are slightly larger and without core-shell structure.

To investigate the influence of biomolecules to BNC morphology, SEM and AFM measurements were performed. Figure 25 shows the SEM images taken from the colloidals of Exp. 1 and Exp. 3.

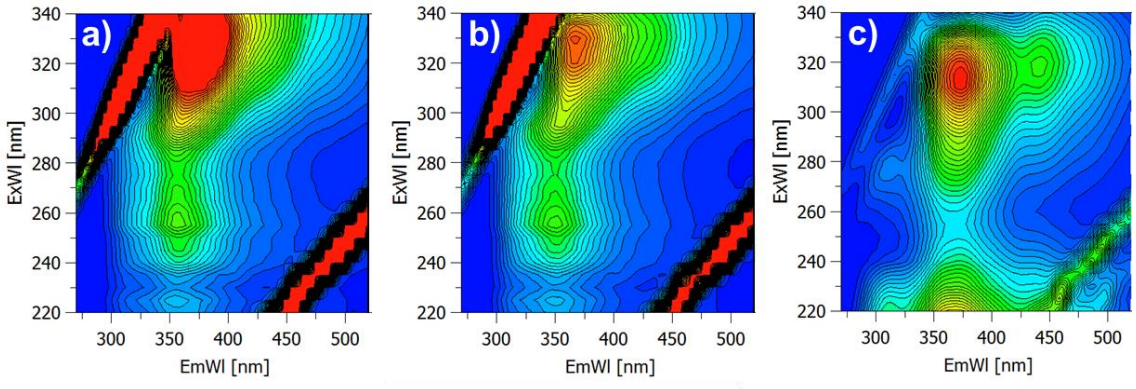

Figure 24 Comparison of fluorescence spectra of a) cocoon of Exp. 6, b) cocoon of Exp. 5, c) solution of Exp. 5.

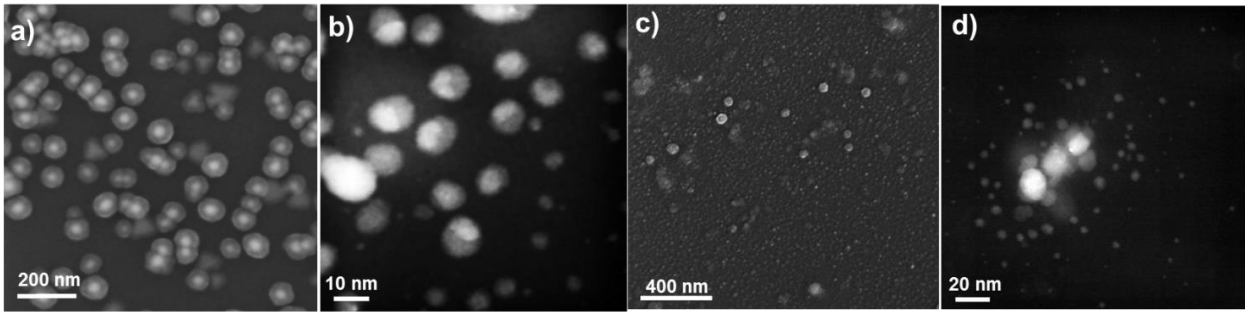

Figure 25 a) SEM and b) TEM image of the colloidal solution of Exp. 1 BNCs c) SEM and d) TEM image of the colloidal solution of Exp. 3.

The reason of specific structure of the particles at different pH conditions could be related to their respective shell density. We assume that at acidic conditions, BNCs have thicker biomolecule shell encapsulating the nanoparticles.

Further investigation through TEM, reveals the inhomogeneity in particle size and lower yield of Exp. 3 colloidal solution. For both, Exp. 1 and Exp. 3, particles down to 5 nm were observed, that are hardly visible in SEM images.

Diffraction pattern of both samples revealed a cubic fcc lattice structure. The *d*-values of nanoparticles are in harmony with the literature (Table 9). Diffraction patterns of both samples as well as a simulation of cubic fcc lattice can be seen in Figure 26. In addition to the surface image techniques AFM was also performed. As shown in Figure 27 the colloidal particles of Exp. 3 are around 20 nm and almost monodisperse. On the other hand, for the colloidal BNCs of Exp. 1 the particle size varies between roughly 15 to 42 nm. This contradictory result compared to results of SEM and TEM might be due to sample preparation or due to the thick protein shell of the acidic

samples, leading to the inhomogeneity. If the concentration of the precursor increases to 20 mM at acidic pH (Exp. 19), the particle size increases gradually. At the same time, instead of core-shell structure, chunky structures with irregular shapes are formed (Figure 28). A further increase of the precursor concentration to 50 mM (Exp. 21), as indicated in Figure 29, increases the nanoparticle size to several micrometers.

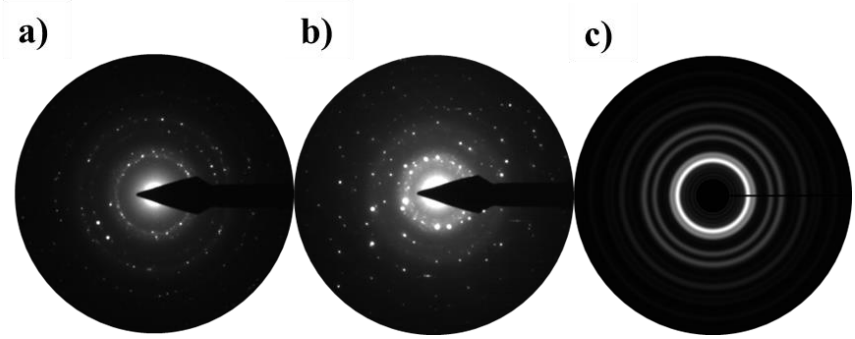

Figure 26 Diffraction pattern of colloidal solution of a) Exp. 1, b) Exp. 3 samples and c) simulation.

Table 9 *d*-values of silver nanoparticle in the literature and synthesized nanoparticles at Exp. 1 and Exp. 3.

d_{pH3} (nm)	d_{pH9} (nm)	d_{lit} (nm)	(*h*,*k*,*l*)
0.233	0.228	0.232	(1,1,1)
0.201	0.203	0.200	(0,0,2)
0.144	0.143	0.142	(0,2,2)
0.121	0.124	0.121	(1,1,3)
0.091	0.092	0.092	(1,3,3)

At first sight these structures seem free of any biomolecule, *i.e.* protein, but when they are irradiated by high energy electron beam of SEM, the upper layer burns out leaving smaller particles underneath (see Figure 29). This proves that the small particles formed at this pH are aggregated and surrounded by biomolecules (Figure 29b).

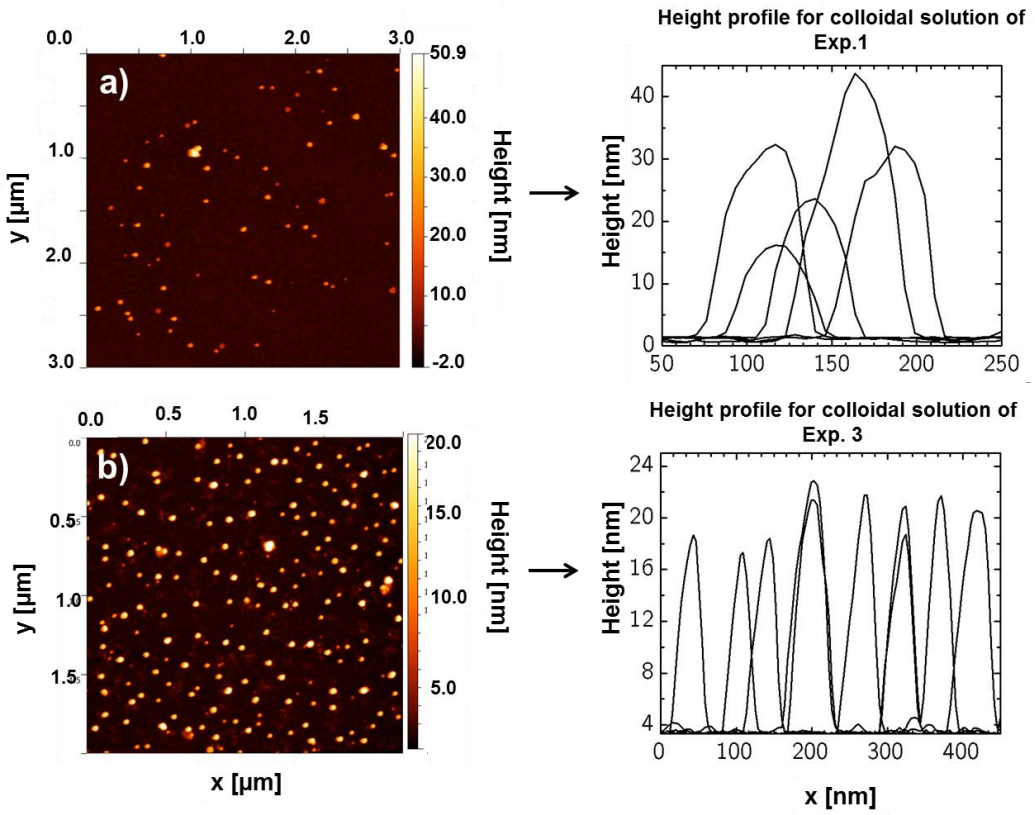

Figure 27 AFM image of colloidal solutions of a) Exp. 1 and their height profile b) Exp. 3 and their height profile.

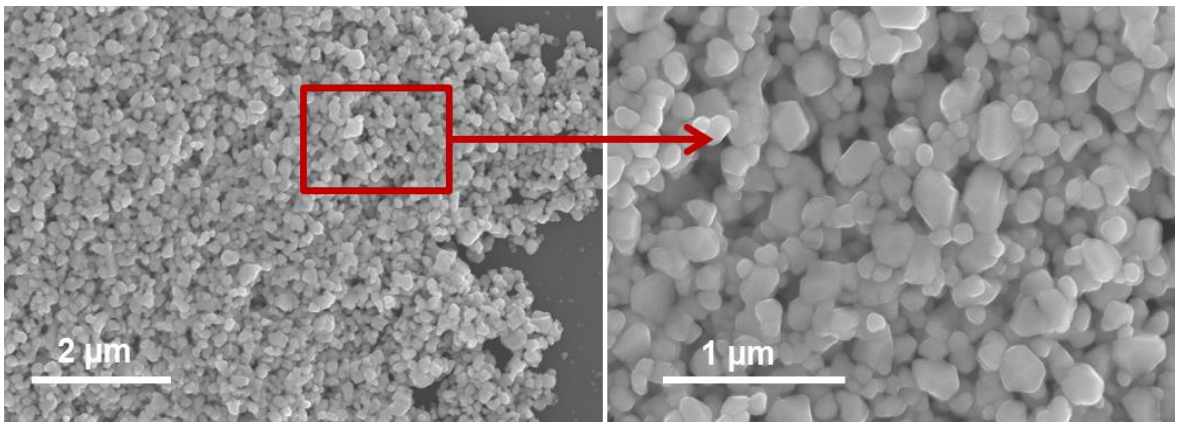

Figure 28 SEM image of the colloidal solution of Exp. 19.

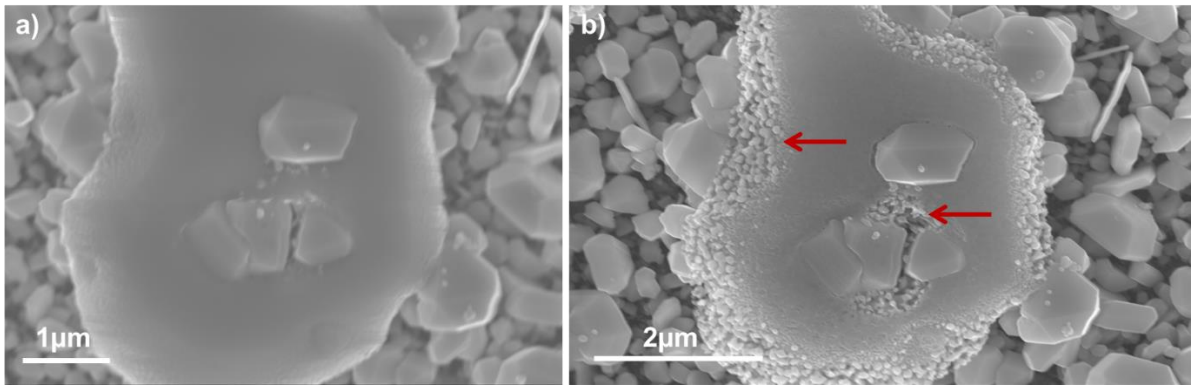

Figure 29 SEM image from the colloidal solution of Exp. 21. Red arrows showing the protein layer burning out due to irradiation of high energy electron beam of SEM.

3.3 Effect of temperature, concentration of metal salts and sericin to BNC production

The sericin release can be influenced by temperature. As the temperature is increased higher molecular weight portions as well as a higher release rate are expected [55]. To verify this assumption, the sericin release at different time intervals and temperatures was monitored. Upon the release, they were exposed to $AgNO_3$ solutions to determine their redox capacity.

This characterization was performed via UV-Vis spectrometry. Figure 30 shows the sericin release at different times at room temperature (Exp. 15) and at 50°C (Exp. 16). The peak at 275 nm - representing the aromatic amino acids- shows slightly higher intensity for Exp. 16. In both experiments, peak intensities have an increasing trend up to 48 hours. However, for Exp. 15 the sericin release from 72 hours (Exp. 15k) had an intensity drop. The reason could be that different molecular weight sericins are released at varying temperatures which will directly affect the synthesis. Perhaps the sericin released at colder environment was not able to sustain homogeneously in water and either they aggregated or gelated after 48 hours.

After blending sericin solutes with a silver nitrate solution, the highest absorption intensity is seen for the 48 hour soaked samples at both temperatures (Exp. 15j, Exp. 16j). Compared to the samples soaked for a shorter time, unexpectedly for Exp. 16 the 72 hour soaked samples showed less intense peaks whereas sericin had already demonstrated high intensities at this temperature and timing. The probable reasons could be: 1) at higher temperature release, the amino acids loose slightly their reducing capability or 2) the molecular weight of the sericin released at that time interval is not suitable for the synthesis. The UV-Vis results of all mixtures are not demonstrated here,

however to show the common behavior, only the results correlated to two and 48 hour soaked samples at both temperatures will be presented (Figure 31, Figure 32).

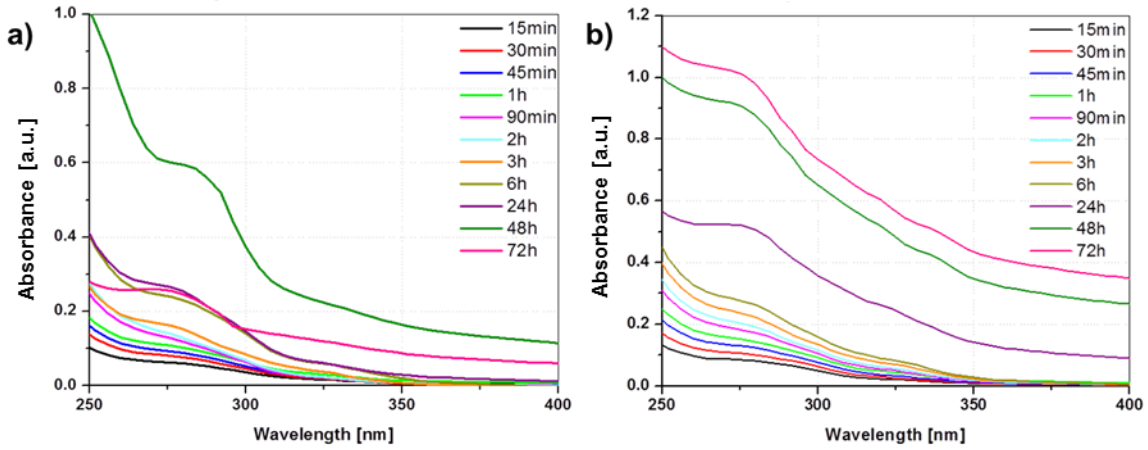

Figure 30 UV-Vis absorption spectrum of sericin release at time intervals indicated for a) Exp. 15a-k, b) Exp. 16a-k.

For the release at 50°C, however, the absorption intensities increased regularly with the reaction time. This implies when temperature slightly increases, the sericin release is enhanced and the nanocomposites can be produced with a higher yield. The intensities for the synthesis made with 1 and 10 mM $AgNO_3$ can be seen in Table 10.

Another interesting observation was about the peak positions. The absorption peaks of the Exp. 16 showed more consistency, and was located around 440 nm with slight shifts over the entire reaction time. Nanoparticles from Exp. 15, on the other hand, showed slight variations and broader absorption peaks. Since the width of a plasmon peak can correlated with particle size and distribution, it is interpreted that the room temperature synthesis brings about more inhomogeneity in particle size and formation of slightly bigger particles. Accordingly, the best conditions of the sericin release include higher temperatures and 48 hours soaking time.

We further investigated the effect of higher concentration of the precursor and the temperature to nanoparticle formation for our “one pot” synthesis at acidic conditions (Exp. 17-21). At acidic pH, the obtained plasmonic solution was green in a four-week course. However, heating the system up to 50°C accelerated this coloration process from four weeks to two days. A visual change in the

color intensity of the solutions with time and temperature can be seen in Figure 33. Needless to say, temperature can act as a catalyst to speed up the reactions.

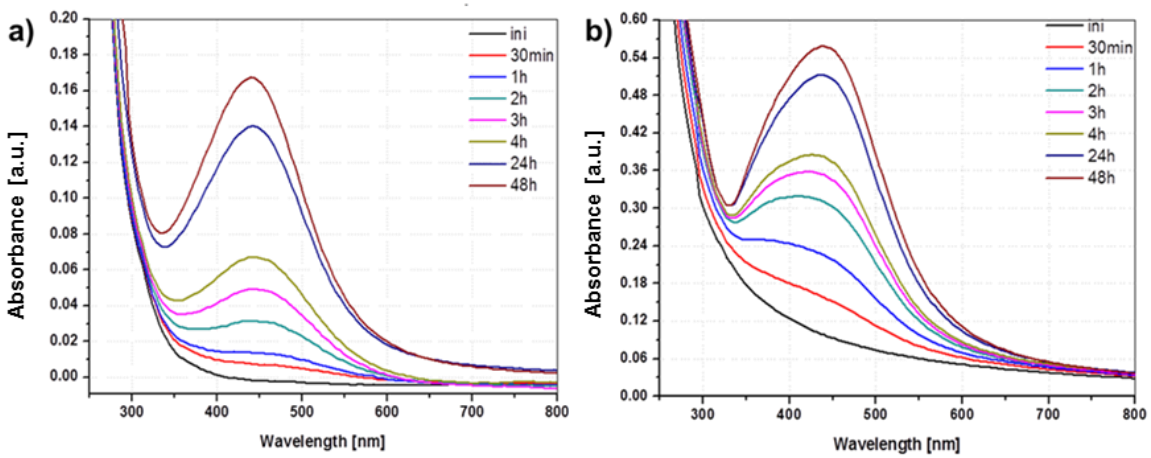

Figure 31 UV-Vis absorption spectrum recorded within 48 hours of synthesis from of nanoparticle formation for a) Exp. 17h, and b) 17j.

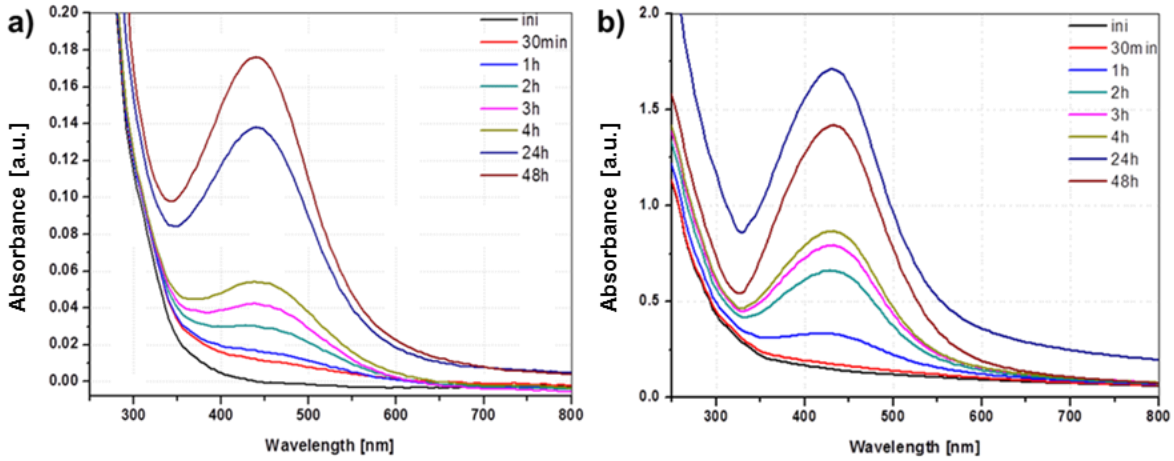

Figure 32 UV-Vis absorption spectrum recorded within 48 hours of synthesis from of nanoparticle formation for a) Exp. 18h, and b) 18j.

When the concentration of the precursor increased, a higher metallic shine on cocoons was observed. Increasing the molarity of the starting salt solution also increased the adherent film thickness which was a special property observed at acidic pH. We have coated polymer substrates with the adherent solutions of Exp. 20 and Exp. 21 in order to investigate their conductivity. Both

samples were conductive and Exp. 20 showed a photo switchable behavior. This photo-switchability effect will be discussed in more details later.

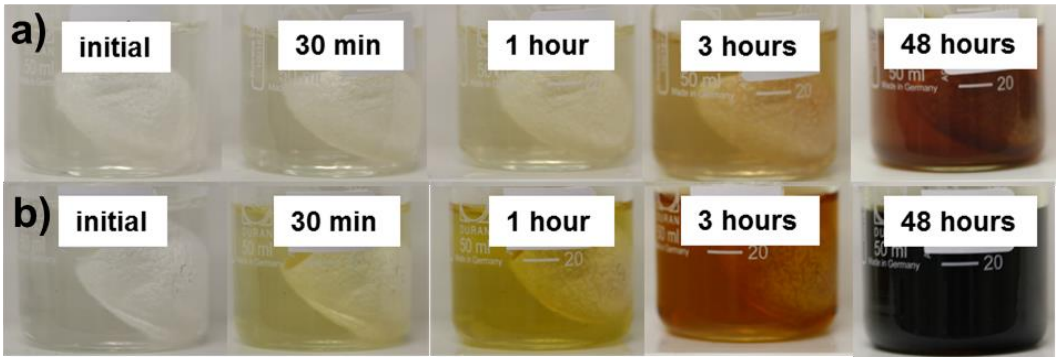

Figure 33 Images after 48 hours of reaction from the solutions of a) Exp. 17 (room temperature), and b) Exp. 18. (50ºC).

Since the sericin solute acts as a reducing/capping agent, its concentration to the synthesis of BNCs should play also a role. To prove this hypothesis different sericin solute to silver nitrate ratios were employed. The yield of the synthesis was investigated by UV-Vis absorption spectrometry.

Dissolved sericin residues induce an absorption peak at 275 nm, attributed to Tyr. After mixing of the salt solutions and sericin, the peak at 275 nm was diminished gradually and a peak at 428 nm emerged over time. The most stable synthesis in terms of aggregation was obtained at 1 mM salt concentration with the 4:1 (Exp. 11) sericin: silver nitrate mixture. Mixing ratios of 2:1 (Exp. 10) and 1:1 (Exp. 9) at 1 mM salt concentration were stable for a short time and aggregated within 3 months. Experiments done using higher salt concentrations (Exp. 12-14), agglomeration of nanoparticles was inevitable within 24 hours. The reason might be that in our first synthesis method, the release of sericin is so slow that the nucleation of nanoparticles and their capping happen at a slow rate and the system is able to maintain the electrostatic attractions between each bionanocomposite through sustained release of sericin residues. Images of the solutions containing different sericin: $AgNO_3$ ratios are shown in Figure 34 and Figure 35 for Exp. 9-11 and Exp. 12-14, respectively.

Using sericin extract to produce nanoparticles rather than using “one pot” approach, changes the kinetics of the synthesis. For the former one, particle nucleation and growth happens much faster compared to capping; leading to aggregation of nanoparticles due to excessive consumption of

sericin micelles. This reality is clearly shown Table 10 when comparing the absorption peaks emerged after 10 min and 5h. The colloidal solutions of Exp. 12-14 show alternating peak positions. This mode of arrangement of peaks is attributed to the nanoparticles' growth. Thus, colloidals of Exp. 9-11 show stable peaks centered at 430 nm.

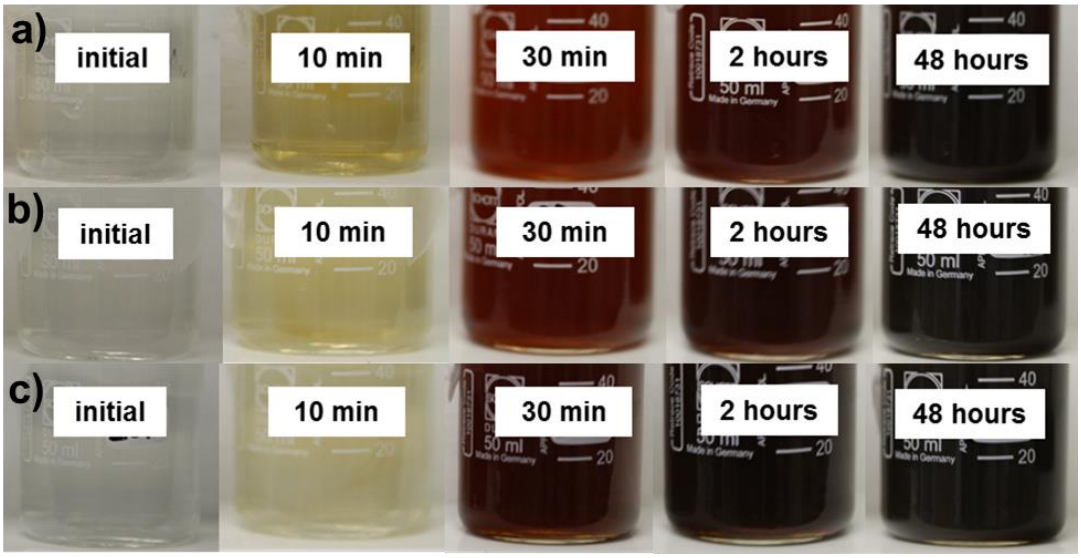

Figure 34 Solutions with different ratios of $AgNO_3$ were prepared: Sericin extract with 1 mM end concentration a) Exp. 9 (1:1), b) Exp. 10 (1:2), and c) Exp. 11 (1:4).

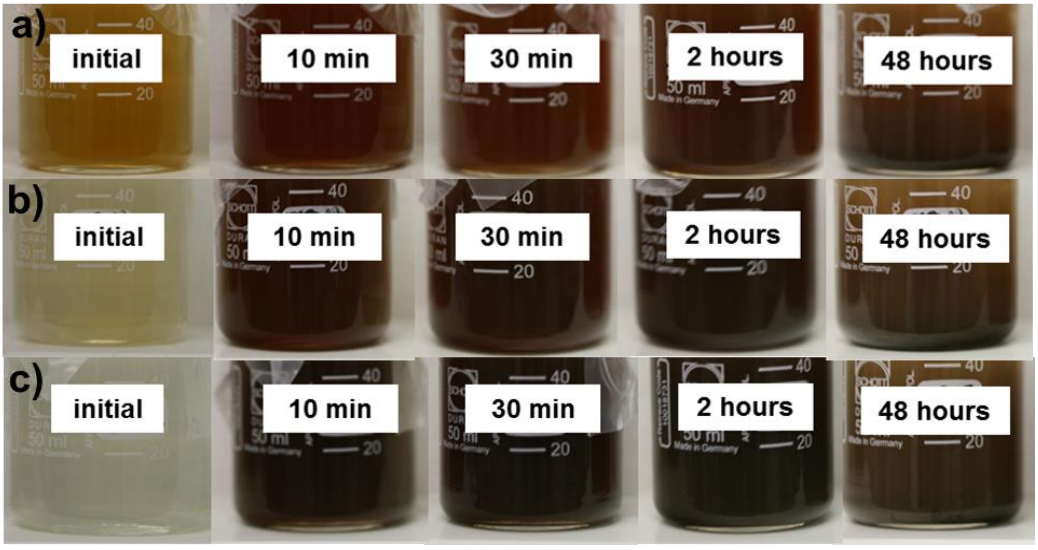

Figure 35 Solutions with different ratios of $AgNO_3$ were prepared: Sericin extract with 10 mM end concentration a) Exp. 12 (1:1), b) Exp. 13 (1:2), and c) Exp. 14 (1:4).

According to these results, the sample of Exp. 12-14 shows an increase in the silver intensity from the start until the first four hours of the synthesis and then it undergoes to aggregation, recognized by naked eye as well as the drop in the absorption intensity. For Exp. 9-12, however, the intensities drastically increase until two hours and then the increasing trend declines. In both cases the higher sericin ratio brings about more silver nanoparticle generation.

Table 10 UV-Vis absorption peak positions for Exp. 9-14, synthesis after 10 min and 5 hours.

Experiment	Peak position after 10 min of synthesis [nm]	Peak position after 5 h of synthesis [nm]
Exp. 9	450	460
Exp. 10	453	465
Exp. 11	452	468
Exp. 12	430	
Exp. 13	430	
Exp. 14	430	

This experiment clarifies the role of sericin concentration in the synthesis. Depending on the required final product, it is possible to accelerate the reaction or increase the yield by changing the sericin ratio in the system.

By using proper concentration of sericin and silver salt, the production can be scaled up to liter volumes within very short times. An example of a volume of 4 liters were prepared within 40 minutes as shown in Figure 36.

Figure 36 4 litres of BNC solution made using sericin extract and $AgNO_3$.

After discussion about the production mechanism of the BNC solutions, we switch to the characterization of the cocoons. A digital image of the bare cocoon and a cocoon of Exp. 1 are illustrated in Figure 37. As shown in this figure, the whole cocoon is homogeneously covered by silver nanoparticles. Figure 38 shows SEM image from fibers of the cocoon of Exp. 19. As seen here, whole fiber surface is totally covered with nanoparticles, justifying the relevant strong metallic shine.

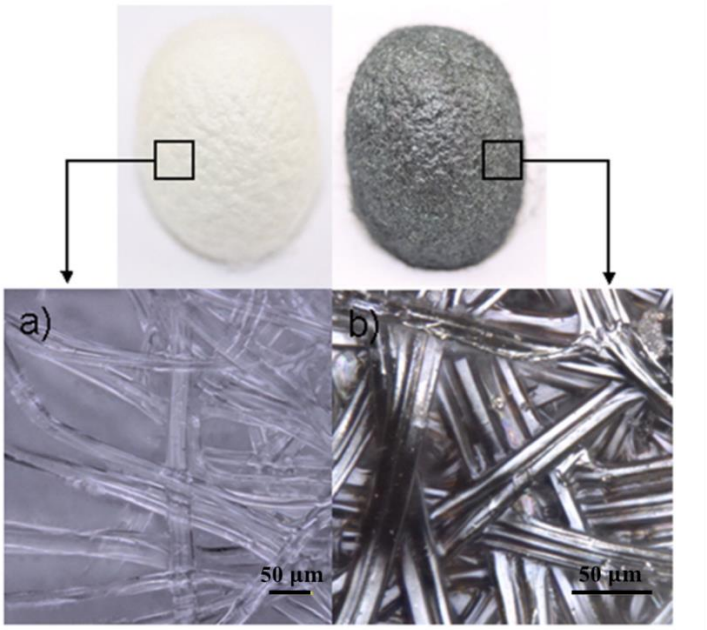

Figure 37 Digital (upper layer) and optical microscope (lower layer) images of a) bare cocoon b) metallic cocoon of Exp. 1.

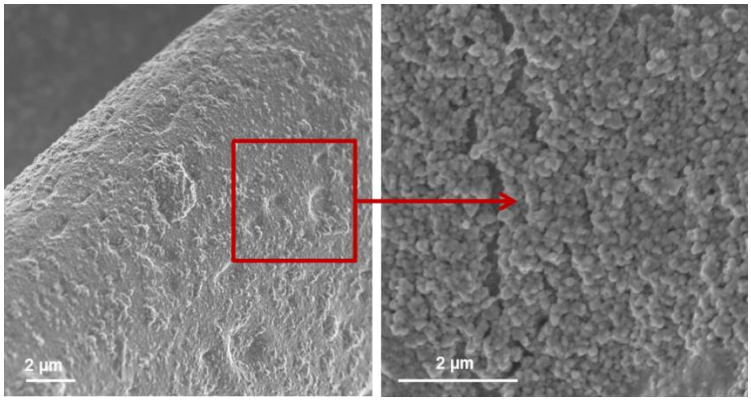

Figure 38 SEM image from the cocoon fibers of Exp. 19.

3.4 Gold bionanocomposites made through the Bioshell concept

To synthesize gold BNCs, the influence of pH, temperature, and concentration of $HAuCl_4$ and alcohols were investigated. UV-Vis measurements demonstrated that all the parameters mentioned, have an important contribution in the yield of the synthesis as well as on the particle size. Assuming that, for reduction process of Ag^+ to Ag^0 only one electron is transferred. However, for Au^{+3} the reaction would have two intermediate stages in order to be reduced to Au^+. Therefore, reduction of gold cations are more complicated compared to silver.

We used varying concentrations of $HAuCl_4$ for the nanoparticle synthesis. Among our experiments the most promising synthesis achieved at 0.1 mM (Exp. 24- 26) and 1 mM (Exp. 27-30) precursor concentrations. At low precursor concentration nanoparticle synthesis at room temperature were unsuccessful. However, by heating up the solutions nanoparticles with pink-red plasmonic colors were obtained at varying pH values. The UV-Vis absorption spectra and the optical images of the solutions can be seen in Figure 39. As seen here, colloidal solutions of Exp. 24 to 26 gave pale pink plasmonic colored solutions. Without any pH correction a narrow absorption peak at 536 nm for Exp. 24 achieved. As the pH modified to more acidic values a broader peak indicating heterogeneous nanoparticle synthesis observed (Exp. 25). Increasing the synthesis temperature at acidic conditions increased the yield of the synthesis however did not influenced the heterogeneity (Exp. 26). For higher salt concentrations, at acidic pH values, at room temperature (Exp. 27) a peak around 550 nm appeared which shift slightly to higher wavelengths and increased in intensity as temperature raised (Exp. 29). For Exp. 28, at elevated pH value a very broad absorption peak with the least intensity observed. As last isopropanol (500 µL) was added to the same sample at acidic pH, the solution's color was intensified and a peak at 576 nm appeared. As seen in this preliminary results regarding to gold synthesis with bioshell technique, the synthesis is favored at acidic pH rather than alkaline conditions and as expected temperature and alcohols helps to increase the yield of the synthesis.

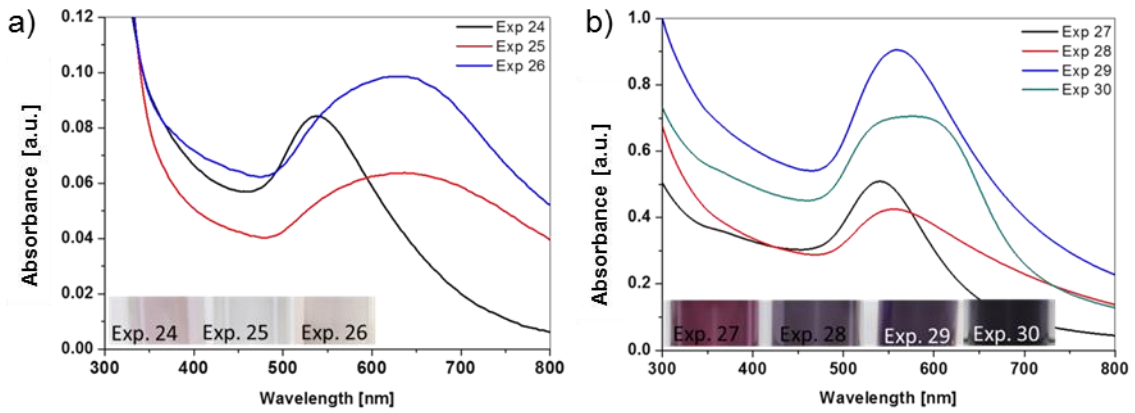

Figure 39 Gold nanoparticle synthesis at a) 0.1 mM precursor concentration, and b) precursor 1mM concentration

4. Applications

In this part, the potential applications of the BNCs made via our bioshell synthesis will be discussed. These applications include coating, ion detection, cancerous cell detection and conductive films.

4.1 Adhesive behavior of the BNCs at acidic conditions

At acidic condition synthesis, the BNCs were able to adhere onto any kind of substrate by simply dipping into solution or in any way of contact for couple of seconds (Figure 40). As the exposure time increased, the coating film thickness was also increased gradually. The method is so effective that even curved surfaces such as tubes can be successfully coated with these particles.

Since silver nanoparticles are known to be antibacterial, this property would be very useful for coating of medical devices such as implants, catheters, surgery utensils having complicated structures.

A study done at Robert Wood Johnson University Hospital Hamilton, showed that almost 40% of healthcare associated infections (HAI) are urinary tract infections thereof 90% are caused by catheter associated urinary tract infections (CAUTI) [56]. To reduce this high ratio of infection risk from catheters, they devised silver coated catheters. Such catheters reduced the infection down to three times less. Yet, the production cost increased about $28,702. As shown from that example as well as the functionality, cost is a huge issue to consider. At this point the BNCs synthesized with our technique would not only cut the production cost compared to conventional synthesis methods but also adds functionality to nanoparticles. Our products encapsulated with biomolecules, due to their potential biocompatibility would be considered as a proper interface between body-silver and catheter.

In order to investigate the endurance of adherent product achieved via Exp. 1 to oxidizer, we subjected the samples coated with the solution of Exp. 1 to H_2O_2. To do so, five beakers were half filled with colloidals of Exp. 1 and 10µL of H_2O_2 were added to each beaker (at different concentration for each beaker). The calorimetric changes over time were recorded. After some time, the nanoparticles of the solution were completely adhered to the glass walls with different coloration depending on the peroxide concentration.

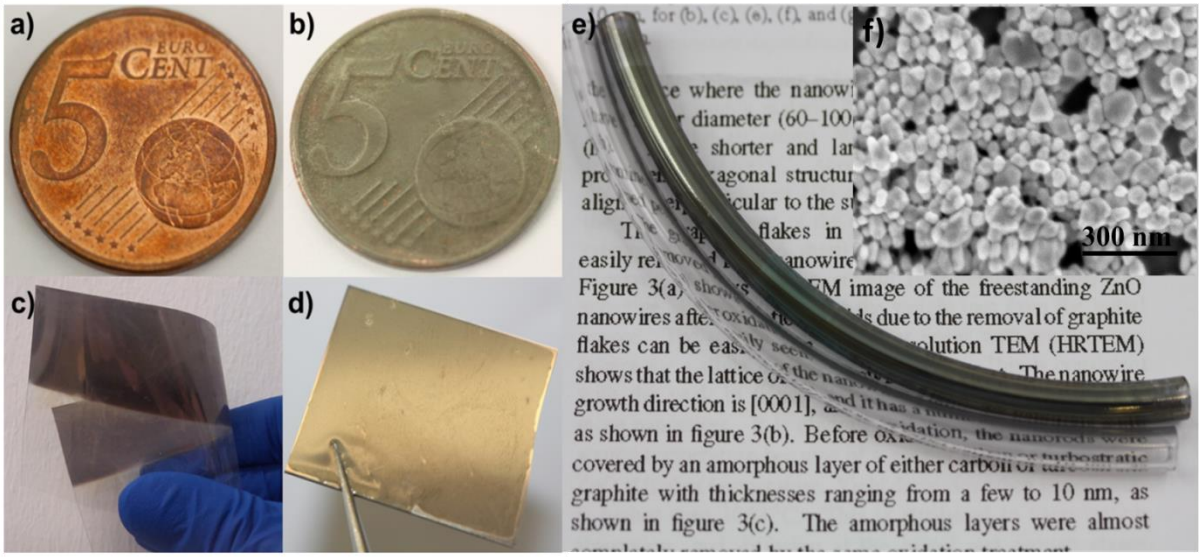

Figure 40 Materials coated with solutions of Exp. 1 showing homogeneous nanoparticle coating for a) bare coin, b) a coin after short term exposure, c) on a flexible plastic sheet after short term dipping, d) on a glass substrate after minutes of exposure e) in a PS tube simply by pouring the solution through the tube f) An SEM image of BNC coating.

Optical images showing calorimetric effects of different H_2O_2 concentration are shown in Figure 41. The adhesion behavior is totally efficient and the coating remains intact even after exposure to some oxidants.

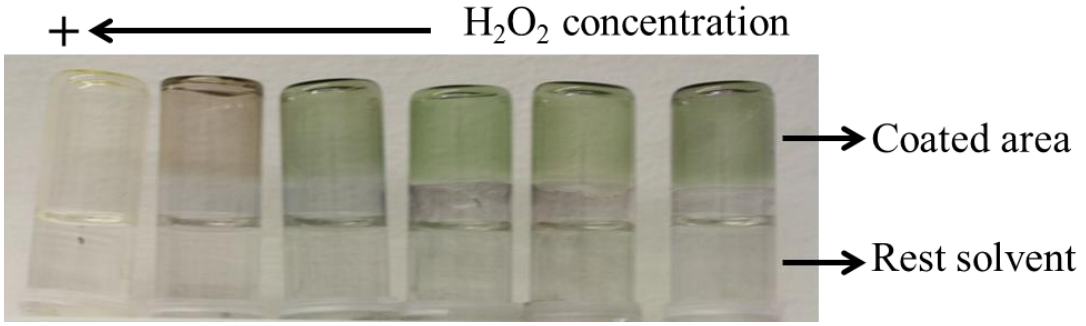

Figure 41 Inverted bottles after H_2O_2 treatment of the acidic BNC solution. The H_2O_2 concentration is increased from left to right.

4.2 Photoconductive behavior of the BNCs at acidic conditions

The advantage of formation of a dense film of silver nanoparticles enables us to confer conductivity even to fibrous and surface substrates.

4. Applications

The conductivity can be beneficial for applications such as smart textiles or biosensors. Printed electronic materials including conductive silver in combination with other materials is an already commercial product (made by many companies *e.g.* DuPont) [57]. As shown before our BNC solution can adhere on any surface from plastic to metal and glass. Thus, production of a flexible and transparent conductive device should be a feasible task.

The conductivity measurements implied our metal shining cocoons synthesized at acidic pH are conductive even when they are produced at lowest molarities. In contrary, the other cocoons produced at alkaline conditions were poor conductors. The conductivity of the samples coated using colloidal solutions synthesized at different concentrations and the cocoon samples investigated in terms of conductivity. As the concentration of the salt solution increases so does the conductivity. For the synthesis at the lowest molarity, the conductivity of the substrates covered and the cocoon itself is as low as nano ampere. Conductivity measurements were also performed while in situ illumination of UV and white light.

Light can increase or decrease the materials conductivity depending on the creation/depletion of mobile charge carriers. For the increased conductivity which can be termed as positive photo conductivity mobile charge carries are increased in the valance band if holes are the major charge carriers and in the conduction band if electrons are the major the charge carriers. In negative photo conductivity, on the other hand, the total number of charge carriers or their life time is diminished by light illumination. This phenomenon is explained by the Stockmann model. In this model, forbidden gap in the material is assumed to have two energy levels; one between the Fermi level and the conduction band and the other closer to valance band which has high capture cross section for electrons and holes. During light illumination electrons from the conduction band and holes from the valance band are captured causing decrease in the total charge carriers within the conduction band. Depending on the substrate, our samples showed both behaviors. While the cocoons covered with silver nanoparticles showed positive photoconductivity, the substrates coated with silver nanoparticles demonstrated negative photoconductivity [58], [59].

Illumination of the cocoons with white light, increased the current drastically. This behavior was reproducible for many cycles. As seen in Figure 42b, current increases over time and reaches a saturation and if the white light is switched off it jumps back to its initial current.

Interestingly, the substrates covered with colloidal solutions of Exp. 1 and Exp. 20 showed negative photoconductivity. In one of our experiments, we covered plastic substrates with the colloidal solutions of Exp. 1, then measured the *I-V* behavior with and without white light illumination. As shown in Figure 43 the current was drastically reduced when the sample was exposed to white light. This behavior was reproducible, though after each cycle the saturation point dropped.

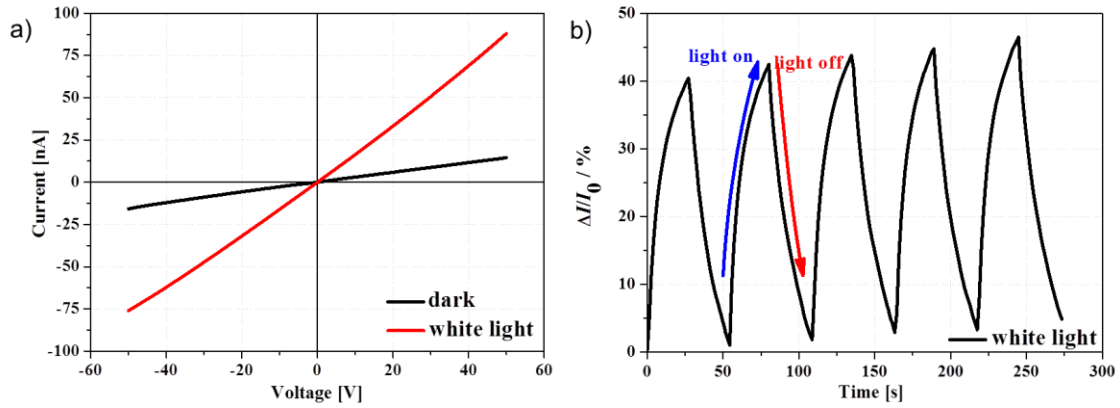

Figure 42 *IV* curve from the cocoon fibers of Exp .1 and b) photocurrent.

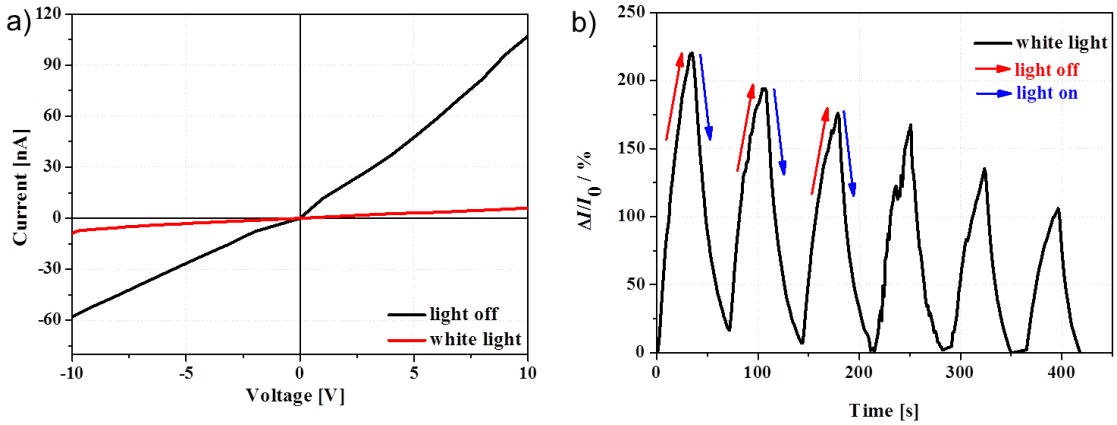

Figure 43 a) *IV* curve and b) current vs. time for exposure to white light: for the plastic substrates coated a negative photocurrent was measured for the colloidal solution of Exp. 1.

We also measured the *I-V* changes for plastic substrates covered with colloidal solutions of Exp. 20. The sample was exposed to UV light and negative photoconductivity was recorded (Figure 44).

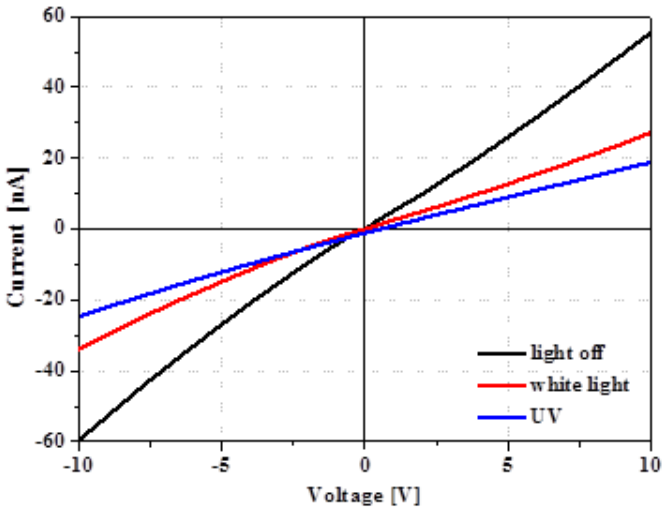

Figure 44 *IV* curve for the plastic substrates coated with colloidal solution of Exp. 20.

4.3 Ion detection by the BNCs at alkaline conditions

The nanoparticles with optical properties such as plasmonic and fluorescence has long been being used in sensoric applications such as detection of heavy ions in body or in drinking water. In this study, a practical approach to ion detection by using our BNCs is presented. Colloidal solutions synthesized at different pH values, colloidals of Exp. 1 and Exp. 4, were used in order to detect different ions. As stated in the experimental part, to do so, different acetate compounds including: lead (II) acetate (Pb(II)Ac), copper (II) acetate (Cu(II)Ac), cobalt (II) acetate (Co(II)Ac), barium (II) acetate (BaAc), iron (II) acetate (Fe(II)Ac), nickel (II) acetate (Ni(II)Ac), manganese (II) acetate (Mn(II)Ac), and cadmium acetate (CdAc), were chosen. The changes in the emission and absorption intensities have been recorded with fluorescence spectroscopy and with UV-Vis spectroscopy, respectively. From the nanoparticle containing solutions, changes within exposure to ions observed only for colloidal solutions of Exp. 4. Colloidals of this experiment was interestingly selective to manganese ions. As shown in Figure 45, emission intensity of Exp. 4 colloidals upon exposure to manganese ions decreased for both excitation values (245 nm, 312 nm), for other ions only minor changes were observed. As stated earlier, this emission peak belongs to dityrosine residues.

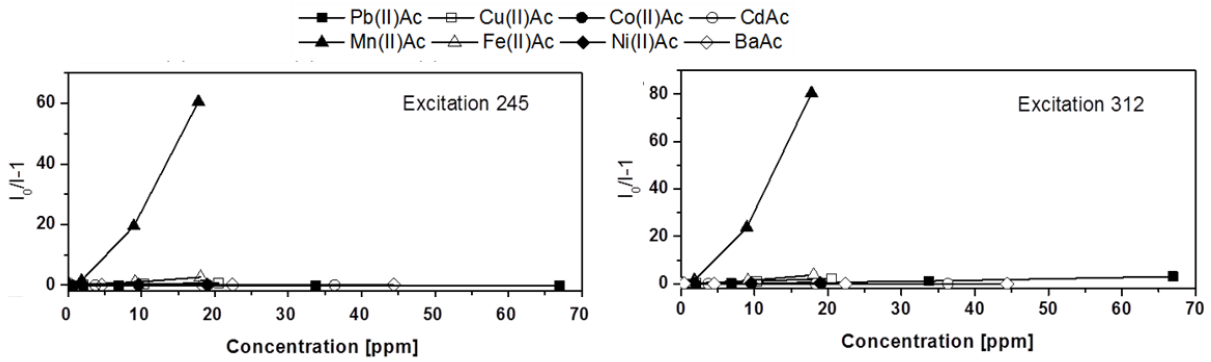

Figure 45 Stern-Volmer plots of emission intensities at 403 nm for excitations at 245 nm and 312 nm for all ions.

The sensitivity of the solution to manganese ions was additionally investigated and found out to be in ppb region. Figure 46 shows the ratio between the original emission intensity and the quenched intensity plotted against manganese concentration in the solutions. As shown, concentration of manganese caused similar changes for both excitation wavelengths.

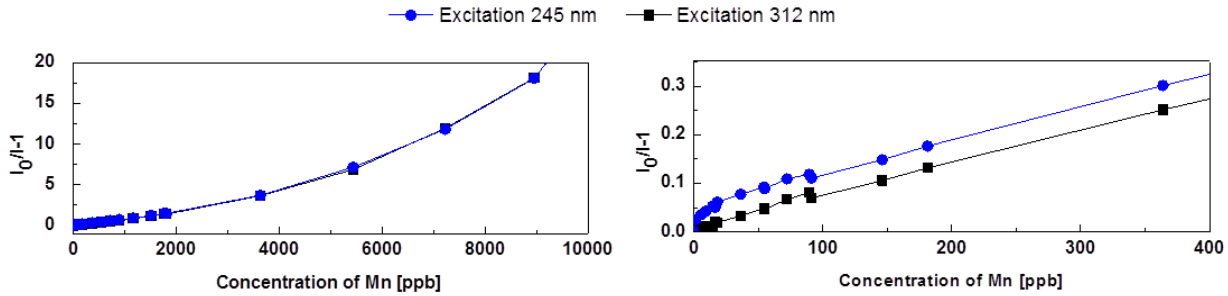

Figure 46 Stern-Volmer plot of the emission intensity at 403 nm with Mn (II) Ac at excitations 245 nm (blue) and 312 nm (black).

The selective calorimetric changes of Exp. 1 and Exp. 4 solutions upon exposure to other ions was rather interesting. The main difference in the synthesis of these two products were their pH, which led to activation of different biomolecules as stated earlier. When we compared the biomolecule release of both solutions the most notable difference is the high dityrosine content of Exp. 4 (which lacks in Exp. 1 solutions). That is why we connected the detection mechanism to presence of dityrosine residues within silver BNCs. We also investigated the effect of Mn ions to reference solution of Exp. 4, and saw that in absence of silver nanoparticles there had been no change observed in the emission intensities.

The color change in the solution was observed even by naked eye. Upon increase in manganese concentration, the color of solution changed from yellow to orange and dark brown (Figure 47a). Figure 47b shows the increase in the absorption intensity is linearly proportional to manganese concentration. According to these outcomes it is proposed that manganese affects the dityrosine bonds between nanoparticles and as a consequence the nanoparticles of the solution undergo aggregation. The aggregated solution shows increased absorption intensity and decreased emission due to lack of dityrosine which would indicate dynamic quenching as explained previously. Yet, due to upward curvature gained from Stern-Volmer plots, it is concluded that dynamic and static quenching are acting in the same time. In order to gain more information about the theory suggested, AFM was performed for the particle solutions in presence and absence of manganese.

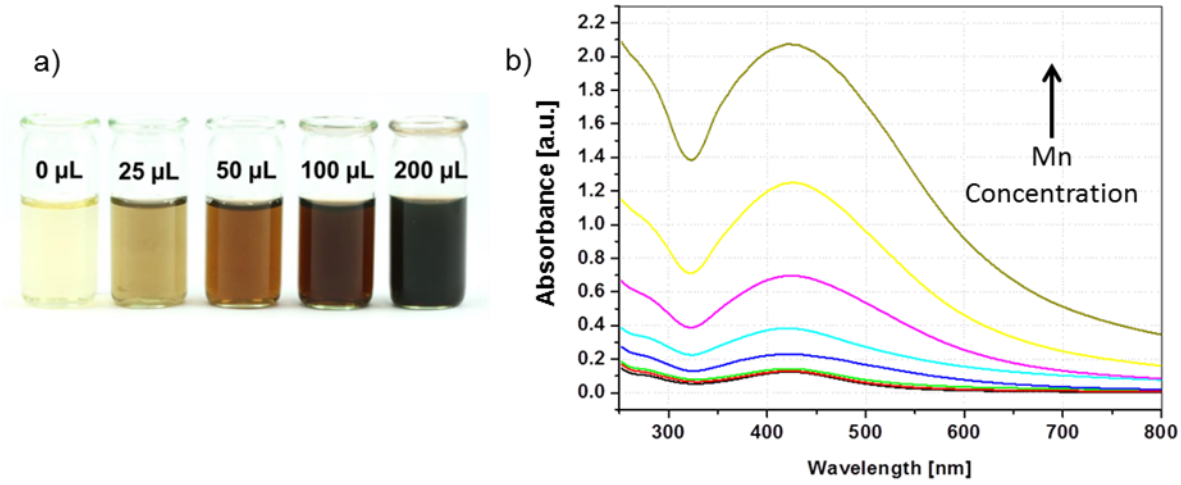

Figure 47 a) pH 11 solution used for detection and addition of Mn (II) acetate solution. The added amounts are as shown on the photo, b) pH 11 solution absorption spectra for different amounts of Mn within solution.

Figure 48a shows the AFM image of the original pH 11 solution. Two observations are noted: the bright spots having heights changing between 2-10 nm attributed to silver nanoparticles and the smaller structures all around the particles which ascribed as organic structures.

When manganese was added (Figure 48b), larger structures emerged up to 180 nm which could be the cause of agglomeration due to destruction of dityrosine bridges. A comparison of the height profiles can be seen in Figure 48a and b.

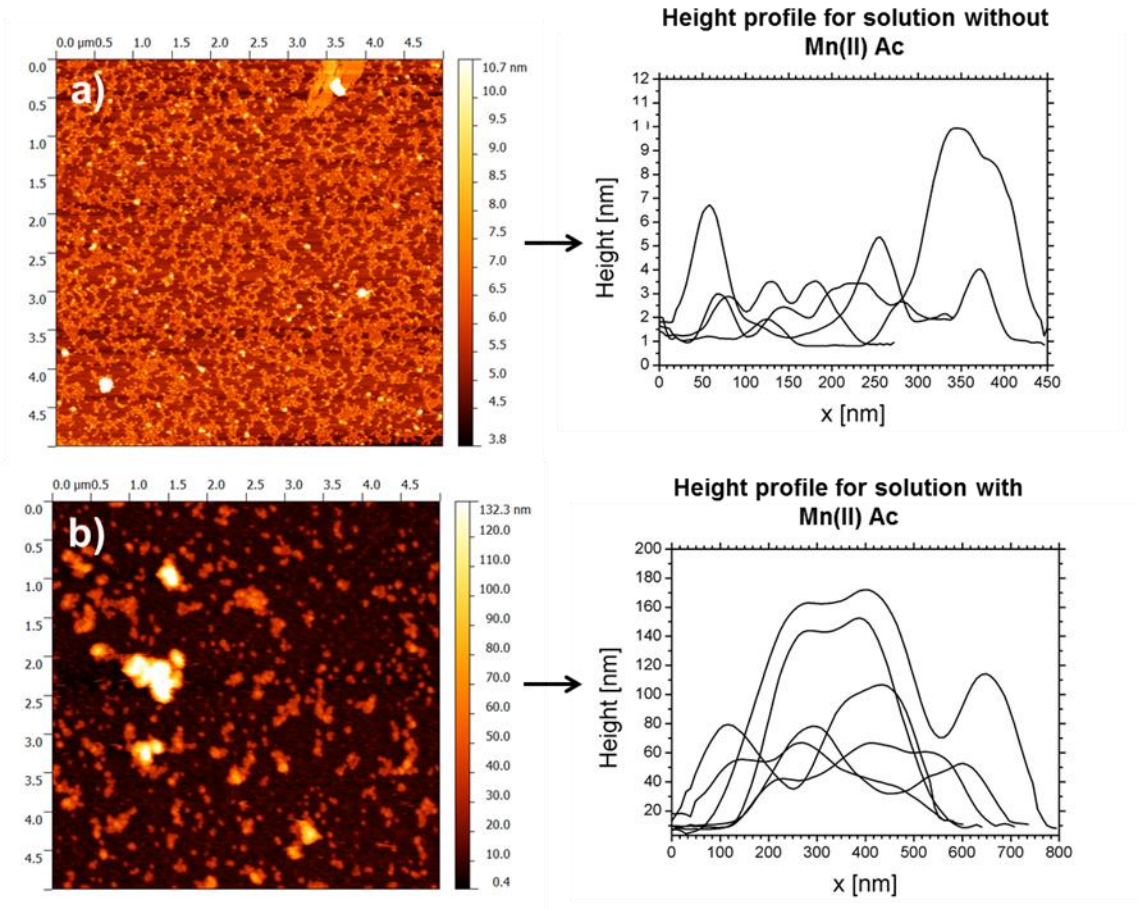

Figure 48 AFM image and height distributions for pH 11 (Exp. 4) solution a) without Mn(II) Ac and b) with Mn(II)Ac.

The selectivity of dityrosine to manganese ions is exceptional. To prove this intrinsic selectivity, the experiment was performed with pH 3 solution, lacking dityrosine and rich in Pyridoxal residues. At acidic condition even at high manganese concentrations no color change of the solution as well as very slight change in absorption spectra is recorded. The UV-Vis absorption measurement as well as corresponding optical images with and without manganese addition to acidic solution can be seen in Figure 49. As shown high amount of manganese added caused slight shift to the absorption spectra and no visible optical change of solutions has been observed. It could be that Pyridoxal residues are as well selectively sensitive to some ions which were not examined within this work.

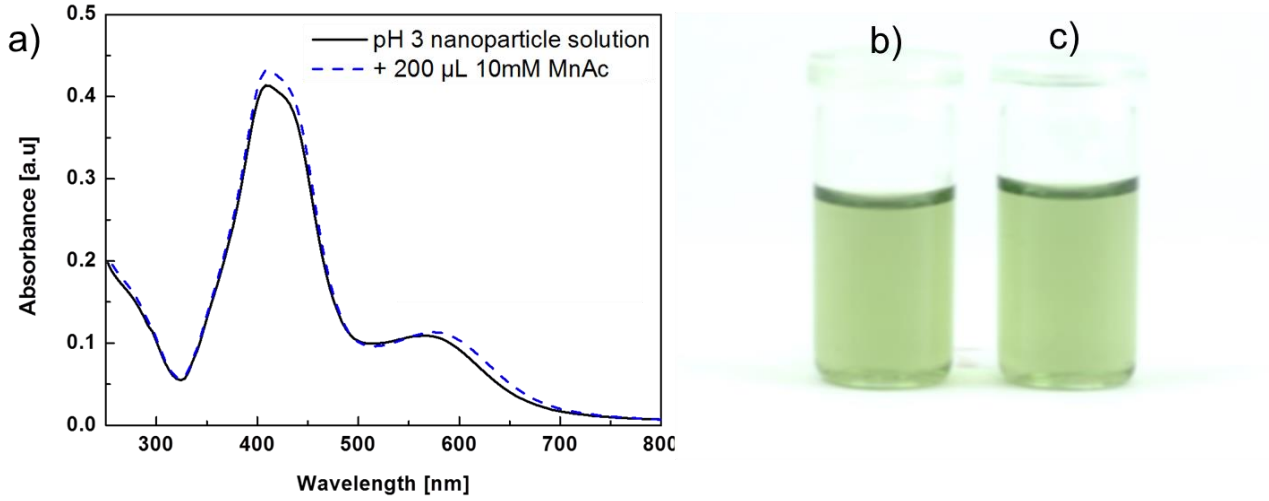

Figure 49 a) Absorption spectra of the pH 3 nanoparticle solution (Exp. 1) with and without MnAc addition, b) BNC solution of pH 3 sample without Mn(II)Ac, and c) with 200 µL of 10mM Mn(II)Ac.

Manganese is one of three toxic essential trace elements [60], meaning that it is needed at certain concentration in order to maintain healthy life, however at high amount it is toxic. In some regions having high Mn concentrations in water, malfunction in children's development has been observed [61]. High intake of Mn as a dietary supplement along with iron is also reported as a risk factor in Parkinson's disease [62].

The technique we used in our work for Mn detection could be a versatile and an economical way to be used in ground water trace element detections or to detect the presence of Mn within the body.

4.4 H_2O_2 detection by the BNCs

Detection of H_2O_2 can be very crucial in some course of diseases including cancer. Cancer cells produce high amount of H_2O_2 and its increase in cellular level has been linked to key alterations in cancer. Some cancer types such as malignant phenotype can be reversed in case of reduction of H_2O_2 cellular levels [63]. Here we show a versatile and cost effective calorimetric/ plasmonic way for detection of H_2O_2 by using our acidic nanoparticle solution. To do so, a stock solution was prepared and then small amount of H_2O_2 was added and continuous UV-Vis measurements as well as optical images were done. Figure 50 shows the optical image of our silver solution before and after H_2O_2 addition at proceeding time intervals. It is clearly seen the green color of the solution decays gradually giving a very pale yellow solution at the last stage. The corresponding UV-Vis

absorption measurements can be found in Figure 51. Here, with the increase of time both plasmon peaks belonging to this solution start to shift to lower wavelengths and in the final stages they faint and after 24 hours no more plasmonic peak is observed. Here our suggestion is that H_2O_2 dissociates to molecular silver to its ions or cause oxidation of the particles which vanishes the plasmonic properties.

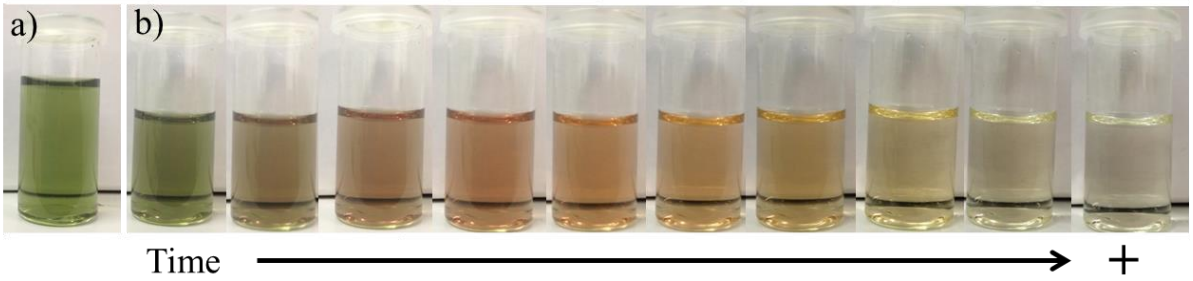

Figure 50 Optical images of a) reference solution and b) plasmonic changes over time after addition of H_2O_2.

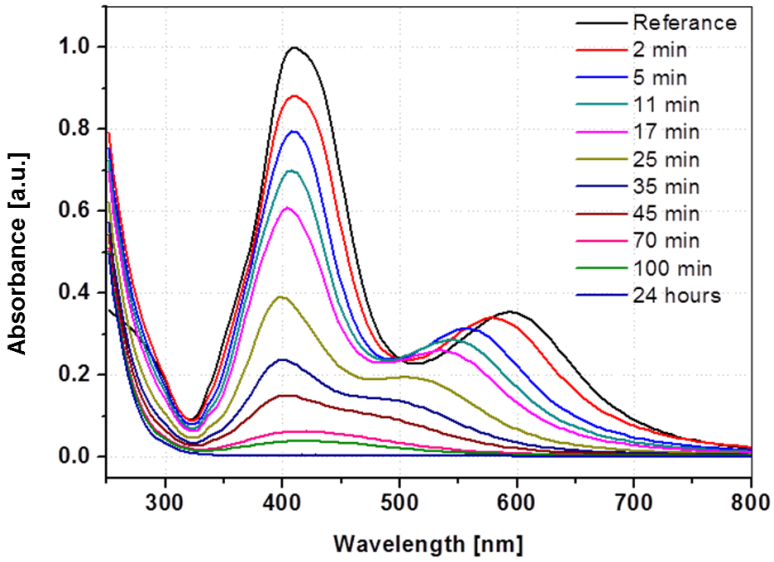

Figure 51 UV-Vis spectra of colloid solution of Exp. 1 before (shown as reference) and after H_2O_2 addition at proceeding time intervals.

5. Summary and Conclusion

In this thesis, the bioshell concept was introduced as a very versatile and easy approach to produce multifunctional bionanocomposites at high yield. Within this concept we have focused on the nanoparticle synthesis using Bombyx Mori silk cocoons. However, the concept was not limited only to cocoons but also extended to other bioshells such as sea urchins, sea snails, starfish and abalones.

Novelty of our technique firstly comes from its simplicity. The bioshells used for synthesis despite the similar techniques presented were used as received. Accordingly, the native forms of bio molecules were protected as much as possible. This approach enables us to synthesize higher yielded and multifunctional BNCs.

The synthesis can be tuned with alterations in pH, temperature and concentration. pH changes lead to release of different bio molecules. At alkaline conditions, the synthesis is driven mainly by aromatic amino acids such as tyrosine and tryptophan however at acidic conditions enzymes such as pyridoxal and NADH are dominant. Alterations in temperature and concentration primarily affect the yield.

The highlight of our research was that compared to other pH values at acidic pH an optimum adhesiveness in the products and also much more yield in production of the BNCs are obtained. To the best of our knowledge, no successful synthesis using cocoons at this condition has been shown before. Also an adhesive composite product out of sericin has been first time shown here up to our knowledge.

We believe that, our simple and cost effective method can be a good solution for problems faced in biology to environment applications, *e.g.* biocompatibility.

As shown here, the main applications of the BNCs lie in the biological area such as ion detection, and photoconductive devices for biology and coating applications.

6. Outlook

The idea and the start point of bioshell concept stems from the need to use economic and environmental friendly -green chemical- synthesis methods.

Our attempts to use green chemical methods were not limited to the bioshell concept. In our research we also used the Leidenfrost approach. By this technique, metal and metal oxide nanoparticles can be synthesized within very short times by using simple laboratory equipment. Here we synthesised ZnO and ZnO_2 nanoparticles due to their attractive and promising use in cancer treatment.

The experiments will be presented in the following were performed in the Institute of Immunology (Universitätsklinikum Schleswig-Holstein), under supervision of Prof. Dr. rer. nat. Dieter Adam. Prof. Dieter Adam and his research group supported us with the valuable immunological information and experiments in order to understand the role of nanoparticles in possible cancer treatment.

The results of this research were not represented within the thesis discussion since it is still at the primary state. However, it is noteworthy to share the results briefly.

In this research we obtained very useful hints about the relationship between size and the chemical composition of the nanoparticles to their toxicity.

We observed that both cancer and healthy cells are more susceptible to ZnO nanoparticles than ZnO_2 ones. Unlike other researches based on ZnO, demonstrating its selective toxicity to cancer cells, [64], [65] in our research no distinguishable selectivity to cancer cells was seen. For ZnO nanoparticles toxicity levels of both particle sizes were similar. Level of toxicity regardless of the cell size has been previously indicated by Lin *et al.* [66]. On the other hand for ZnO_2 we found a clear threshold in cell viability at each concentration for different particle sizes.

Very interestingly, different cytotoxic profiles for suspension and adherent cells for different sizes of ZnO_2 was determined. For suspension cell lines such as “normal” peripheral blood mononuclear cells (PBMCs), leukemic Jurkat T cells and U-937 lymphoma cells, cell death ratios observed by PI staining method can be seen in Figure 52. 126 nm sized nanoparticles created much more toxic effect and caused more cell death. However, for adherent cells lines such as L929Ts (murine

fibrosarcoma), Panc89 (human pancreatic adenocarcinoma), and HT-29 (human colorectal carcinoma) 126 nm particles only at concentration above 200 µg/mL showed higher toxicity. Below 200 µg/mL nanoparticle concentration, 426 nm particles were more effective (Figure 53). For the cell lines of Panc89, and HT29, the investigated nanoparticle concentrations were 50, 100, 200, 500 and 1000 µg/mL. For L929Ts the cytotoxic effects of nanoparticles were very high and above 50µg/mL, all cells were detected as PI positive.

Except L929Ts cells, toxicity (PI positive 50% and more) of ZnO_2 observed between 200-400 µg/mL for both nanoparticle sizes for all cells used. However, for L929Ts cells toxicity observed between 20-30 µg/mL. Moreover, for L929Ts the bigger nanoparticles caused more cell death compared to smaller ones.

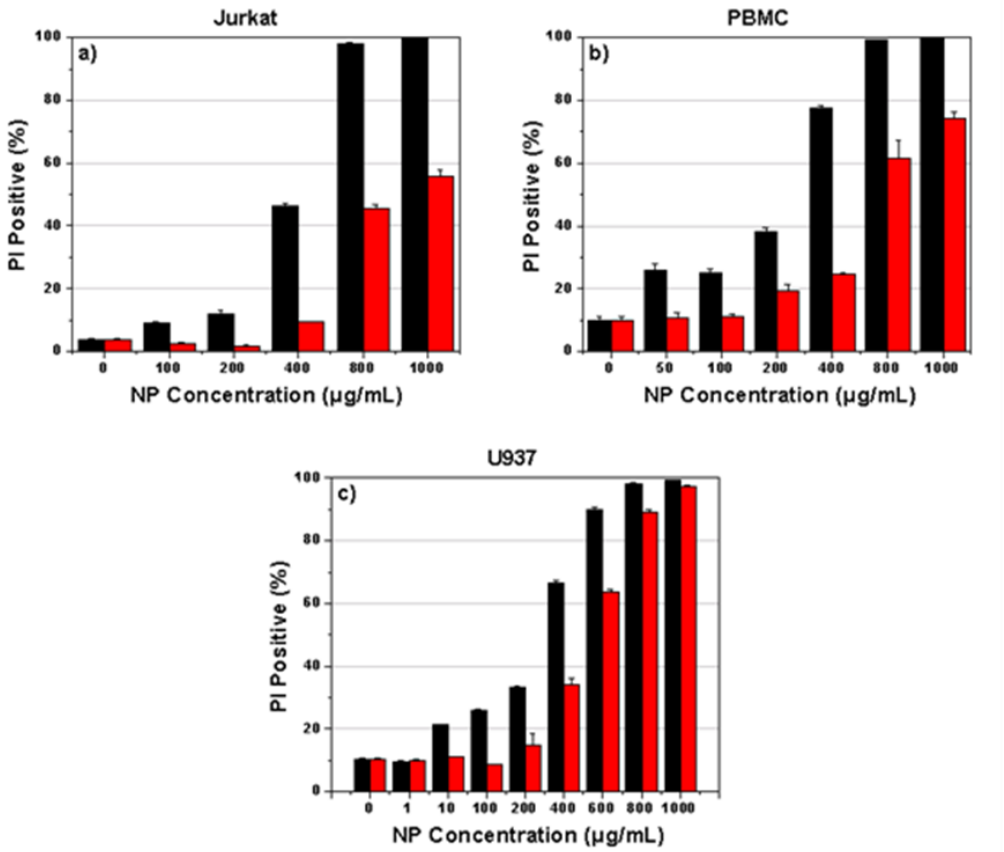

Figure 52 Cell death ratios for ZnO_2 by PI staining a) Jurkat, and b) PBMCs, and c) U937s; Black columns stand for 126 nm red ones for 426 nm particles.

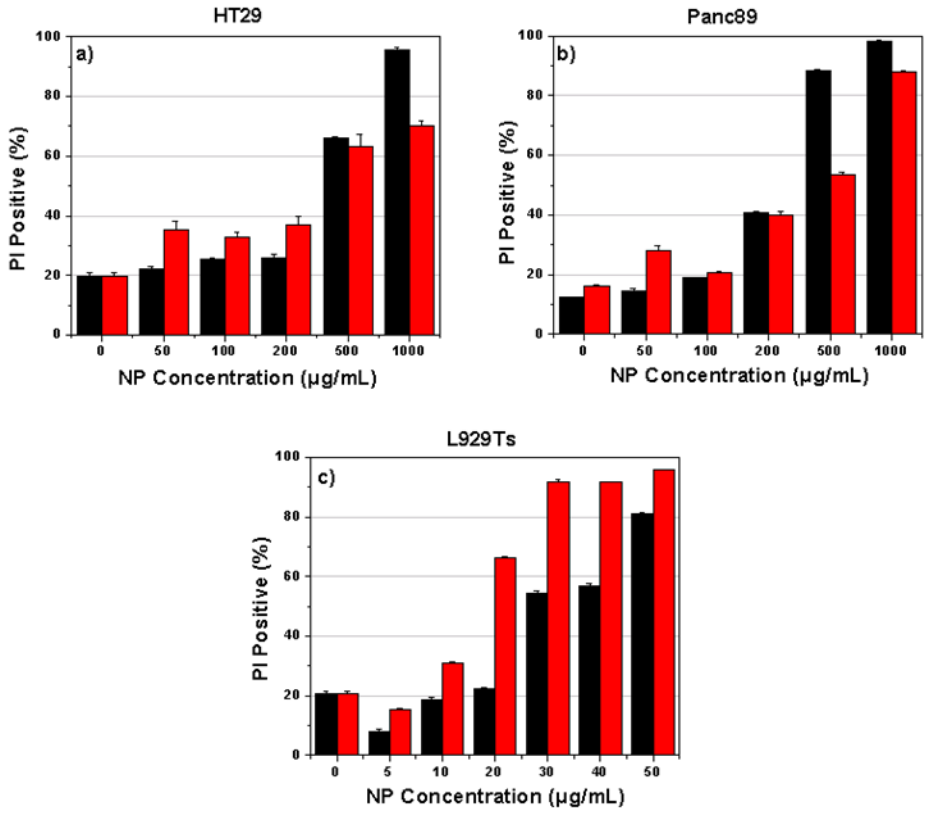

Figure 53 Cell death ratios for ZnO_2 by PI staining a) Ht29, and b) Panc89, and c) L929Ts; Black columns stands for 126 nm and red ones for 426 nm particles.

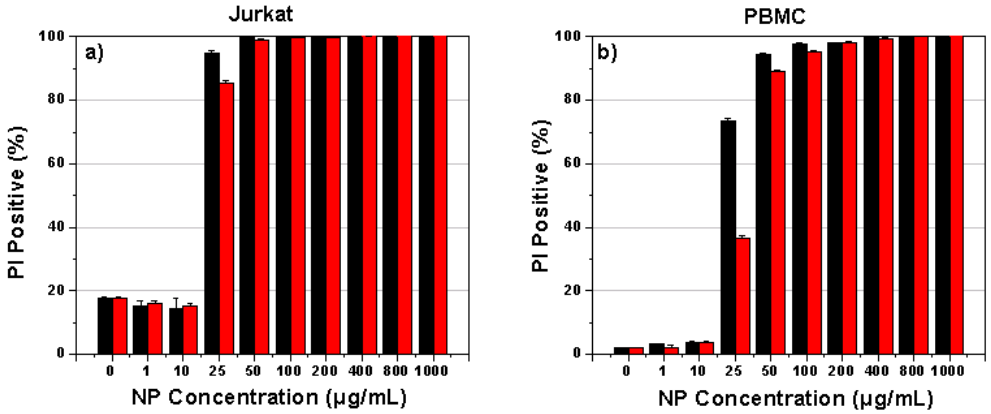

Figure 54 Cell death ratios for ZnO by PI staining a) Jurkat, and b) PBMC; Black columns stands for 126 nm and red ones for 426 nm particles.

The toxicity (PI positive 50% and more) of ZnO for suspension cells of Jurkat and PBMCs, was investigated and found to be between 10-25 µg/mL for both size of nanoparticles (Figure 54).

These results are in harmony with previous studies done by Lin *et al.* [66]. In their research, they used human bronchoalveolar carcinoma-derived cell line-A549 stimulated with 70 and 420 nm ZnO nanoparticles (Sigma) and found the toxicity between 18-25 µg/mL for both sizes.

In this work, also the effect of morphology on the toxicity induced by micron sized ZnO nanoparticles was investigated. The first results are shown in Figure 55.

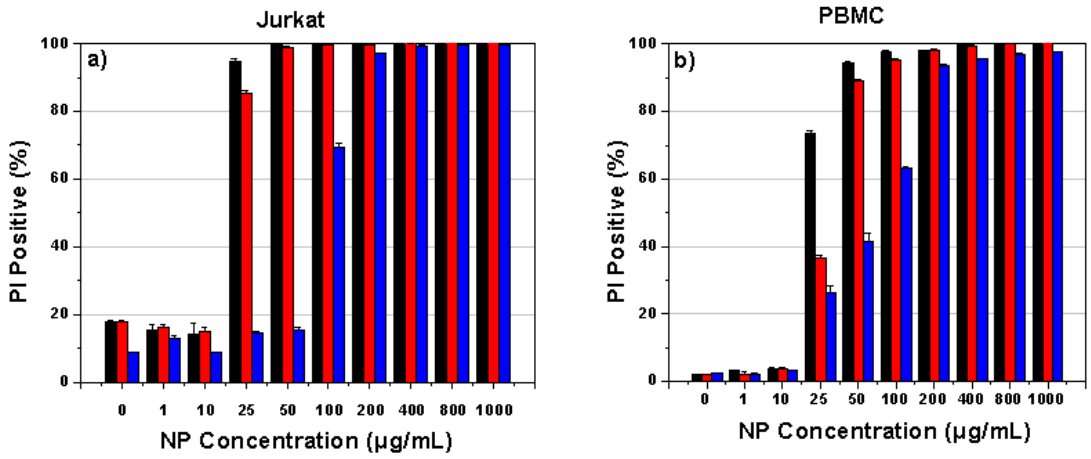

Figure 55 Cell death ratios for ZnO by PI staining a) Jurkat, and b) PBMC; Black columns stands for 126 nm and red ones for 426 nm sized ZnO nanoparticles and blue ones for star-like structures of ZnO.

The results show the micron sized star-like structures indicating much lower toxic effect compared to nano-scaled particles. Still no evidence of selectivity to cell type is observed.

To explore the cell death mechanisms, we investigated the cleavage of poly-ADP ribose polymerase (PARP) in U-937, Jurkat, HT29 and L929Ts cells treated with ZnO_2 nanoparticles (Figure 56). For cells going through apoptosis, PARP-1 is inactivated by caspase-3-dependent cleavage of the full-length 116-kDa protein to an 89-kDa product. For necroptotic cells (e.g. TNF-treated L929Ts cells), PARP-1 displays an atypical size shift/disappearance of the mature, uncleaved protein [67].

According to this assay, all cell lines except L929Ts follow apoptosis. The strength of the 89 kDa band indicates more apoptotic events. The results of this assay coincides with flow cytometer data.

In flow cytometry the smaller nanoparticles showed more toxicity for U937 and Jurkat cell lines and in PARP assay also the cleave band is thicker for smaller nanoparticles. For HT29 cell line

higher apoptotic events recorded above 200 µg/mL concentration with 126 nm particles and below that concentration with 426 nm particles which again coincide with flow cytometry data.

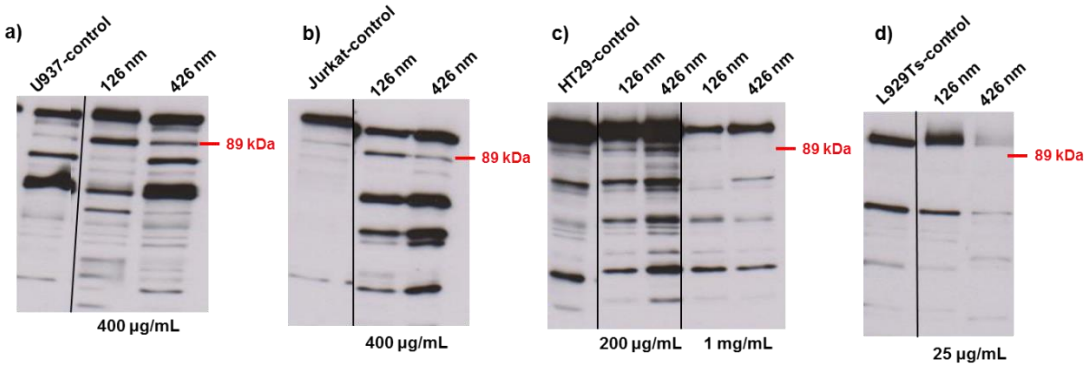

Figure 56 PARP assay for 126, and 426 nm nanoparticles of ZnO_2. a) for U937 cell line at 400 µg/mL; b) for Jurkat at 400 µg/mL; c) for HT29 cell line at 200 µg/mL and 1 mg/mL; d) for L929Ts at 25 µg/mL concentrations.

Contrarily L929Ts indicated necrotic pathway by the absence of 89 kDa band and presence of smeared band of mature, uncleaved protein. The disappearance of this band is due to the PARP activation indicating more activated ones would go through more necrosis. This result as well is in agreement with flow cytometry data where 426 nm particles causing higher cell death.

The fact that smaller particles show greater toxicity has been shown in many studies. As the size becomes smaller, the number of surface atoms compared to volume will be larger. This would bring more probability of surface defects (e.g. Zn, O vacancies), decreased nanocrystal quality and higher electron donor-accepter impurities which in return would potentially generate far more reactive oxygen species (ROS) [36].

In this research, unlike other similar studies stated previously, using ZnO nanoparticles we observed no selective toxicity to cancer cells. The reasons could be as follows: nanoparticles can be produced in various methods and each method supplies different surface characteristics to nanoparticle in terms of chemistry and activity. Since the surface properties are the main active sites in order to create toxicity; it is reasonable to have different results with different production techniques.

6. Outlook

Our next research goal would be production of selective cancer destructors, by modifications in the surface chemistry of nanoparticle. This can be done by functionalizing the particles with some chemotherapeutic drugs or by alternating their surface charge by stabilizers.

Another consideration would be nanoparticle morphology, it is expected that particles at different morphologies might show different actions due to changed active sites and surface area.

Another future work is planned to show ROS generation in cells, the easiest way could be use of an antioxidant such as NAC. For further investigation of cell death mechanism PI/Annexin staining could be additionally done.

Bibliography

[1] S. Horikoshi, and N. Serpone. , Microwaves in Nanoparticle Synthesis: Fundamentals and Applications, John Wiley & Sons, 2013.

[2] F. Raimondi, and G.G. Scherer, and R. Kötz, and A. Wokaun., "Nanoparticles in Energy Technology: Examples from Electrochemistry and Catalysis," Angewandte Chemie International Edition, vol. 44, no. 15, p. 2190–2209, 2005.

[3] Salata, OV., "Applications of nanoparticles in biology and medicine," Journal of Nanobiotechnology,, vol. 2, no. 3, 2004.

[4] K. N. Thakkar, and S. S. Mhatre, and R. Y. Parikh., "Biological synthesis of metallic nanoparticles," Nanomedicine: Nanotechnology, Biology and Medicine, vol. 6, no. 2, p. 257–262, 2010.

[5] P. Mohanpuria, and N. K. Rana, and S. K. Yadav., "Biosynthesis of nanoparticles: technological concepts and future applications," Journal of Nanoparticle Research, vol. 10, no. 3, p. 507-517, 2008.

[6] Alexander, J. W. , "History of the Medical Use of Silver," , vol. 10, 2009.," Surgical Infections, vol. 10, no. 3, p. 289-292, 2009.

[7] Frenzel, G., "The Restoration of Medieval Stained Glass," Scientific American, vol. 252, no. 5, p. 126-135, 1985.

[8] I. Freestone, and N. Meeks, and M. Sax, and C. Higgitt. "The Lycurgus Cup – A Roman Nanotechnology," Gold Bulletin, vol. 40, no. 4, p. 270-277, 2007.

[9] J. Kimling, and M. Maier,and B. Okenve , and V. Kotaidis , and H. Ballot , and A. Plech., "Turkevich Method for Gold Nanoparticle Synthesis Revisited," The Journal of Physical Chemistry B, vol. 110, no. 32, p. 15700-15707, 2006.

[10] E. Abbasi, and M. Milani, and S. F. Aval, and M. Kouhi, and A. Akbarzadeh, and H. T. Nasrabadi, and P. Nikasa, and S. W. Joo, and Y. Hanifehpour, and K. Nejati-Koshki, and and M. Samiei, "Silver nanoparticles: Synthesis methods, bio-applications and properties," Critical Reviews in Microbiology, vol. 42, no. 2, p. 173-180, 2016

[11] Liz-Marzán, L. M., "Gold nanoparticle research before and after the Brust–Schiffrin method," Chemical Communications, vol. 49, no. 1, p. 16-18, 2013

[12] S. R. K. Perala, and S. Kumar., "On the Mechanism of Metal Nanoparticle Synthesis in the Brust−Schiffrin Method," Langmuir, vol. 29, no. 31, p. 9863−9873, 2013.

[13] V. Amendola, and M. Meneghetti. , "Laser ablation synthesis in solution and size manipulation of noble metal nanoparticles," Physical Chemistry Chemical Physics, vol. 11, no. 20, p. 3805–3821, 2009.

[14] M. Hu, and J. Chen, and Z.-Y. Li, and L. Au, and G. V. Hartland, and X. Li, and M. Marqueze, and Y. Xia. , "Gold nanostructures: engineering their plasmonic properties for biomedical," Chemical Society Reviews, vol. 35, no. 11, p. 1084-1094, 2006.

[15] S. C. Kundu, and B. C. Dash, and R. Dash, and D. L. Kaplan. , "Natural protective glue protein, sericin bioengineered by silkworms: Potential for biomedical and biotechnological applications," Progress in Polymer Science, vol. 33, no. 10, p. 998–1012, 2008.

[16] C. Fu, and Z. Shao, and V. Fritz., "Animal silks: their structures, properties and artificial production," Chemical Communications, no. 43, p. 6515–6529, 2009.

[17] M. Mondal, and K. Trivedy, and S. N. Kumar., "The silk proteins, sericin and fibroin in silkworm, Bombyx mori Linn., a review," Caspian Journal of Enviromental Sciences, vol. 5, no. 2, p. 63-76, 2007.

[18] P. Aramwit, and T. Siritientong, and T. Srichana., "Potential applications of silk sericin, a natural protein from textile industry by-products," Waste Management & Research, vol. 30, no. 3, p. 217-224, 2012.
[19] B. Kludkiewicz, and Y. Takasu, and R. Fedic, and T. Tamura, and F. Sehnal, and M. Zurovec., "Structure and expression of the silk adhesive protein Ser2 in Bombyx mori," Insect biochemistry and molecular biology, vol. 39, no. 12, p. 938-946, 2009.
[20] L. A. Burzio, and J. H. Waite., "Cross-linking in adhesive quinoproteins: studies with model decapeptides," Biochemistry, vol. 39, no. 36, p. 11147-11153, 2000.
[21] Hamaguchi, K. , The Protein Molecule: Conformation, Stability and Folding, Tokyo: Japan Scientific Society Press and Springer Verla, 1992.
[22] H. Oh, and J. Y. Lee, and A. Kim, and C. S. Ki, and J. W. Kim, and Y. H. Park, and K. H. Lee. , "Preparation of silk sericin beads using LiCl/DMSO solvent and their potential as a drug carrier for oral administration," Fibers and Polymers, vol. 8, no. 5, p. 470-476, 2007.
[23] P. N. Bhat, and S. Nivedita, and S. Roy., "Use of sericin of Bombyx mori in the synthesis of silver nanoparticles, their characterization and application," Indian Journal of Fibre and Textile Research, vol. 36, p. 168-171, 2011.
[24] S. Nivedita, and P. N. Bhat, and S. Roy. , "Sericin of Bombyx Mori as a Reducing and Capping Agent in the Preparation of Silver Nanoparticles," Séricologia, vol. 50, no. 3, p. 351-354, 2010.
[25] J. L. Ding, and W. Wu., "Green Synthesis of Silk Sericin-Based Silver Nanoparticles," Advanced Materials Research, Vols. 415-417, p. 487-490, 2012.
[26] P. Aramwit, and N. Bang, and J. Ratanavaraporn, and S. Ekgasit., "Green synthesis of silk sericin-capped silver nanoparticles and their potent anti-bacterial activity," vol. 9, p. 79, 2014," Nanoscale Research Letters, vol. 9, no. 79, p. 79, 2014.
[27] Lakowicz, J. R., Principles of Fluorescence Spectroscopy, Springer, 2006.
[28] S. El Qaidi, and J. Yang, and J.-R. Zhang, and D. W. Metzger, and G. Bai, "The Vitamin B6 Biosynthesis Pathway in Streptococcus pneumoniae Is Controlled by Pyridoxal 5′-Phosphate and the Transcription Factor PdxR and Has an Impact on Ear Infection", Journal of Bacteriology, vol. 195, no. 10, p. 2187–2196, 2013.
[29] W. A. Murray, and W. L. Barnes. , "Plasmonic Materials," Advanced Materials, vol. 19, no. 22, p. 3771-3782, 2007.
[30] Liz-Marzán, L. M. , "Nanometals: Formation and Color," Materials today, vol. 7, no. 2, p. 26–31, 2004.
[31] R. Abdelaziz, and D. Disci-Zayed, and M. K. Hedayati, and J. Pöhls, and A. U. Zillohu, and B. Erkartal, and V. S. K. Chakravadhanula, and V. Duppel, and L. Kienle, and M. Elbahri., "Green chemistry and nanofabrication in a levitated Leidenfrost drop," Nature Communications, vol. 4, 2013.
[32] Lenard, P., "Ueber Wasserfallelektrizitaet und ueber die Oberflaechenbeschaffenheit," Ann. Phyc., vol. 352, p. 463-524, 1915.
[33] H. W. Gilbert, and P.E. Shaw., "Electrical charges arising at a liquid- gas interface," Proc. Physc. Soc, vol. 37, p. 195-214, 1925.
[34] S. Nie, and Y. Xing, and G. J. Kim, and J. W. Simons., "Nanotechnology applications in cancer," Annual Review of Biomedical Engineering, vol. 9, pp. 257-288, 2007.
[35] S.-D. Li, and L. Huang., "Pharmacokinetics and biodistribution of nanoparticles," Molecular pharmaceutics, vol. 5, no. 4, p. 496-504, 2008.

[36] J. W. Rasmussen, and E. Martinez, and P. Louka, and D. G. Wingett, "Zinc oxide nanoparticles for selective destruction of tumor cells and potential for drug delivery applications," Expert opinion on drug delivery, vol. 7, no. 9, p. 1063-1077, 2010.
[37] M. Wang, and M. Thanou. , "Targeting nanoparticles to cancer," Pharmacological Research, vol. 62, no. 2, p. 90-99, 2010.
[38] H. Pelicano, and D. Carney, and P. Huang, "ROS stress in cancer cells and therapeutic implications," Drug Resistance Updates, vol. 7, no. 2, p. 97-110, 2004.
[39] D. Trachootham, and J. Alexandre, and P. Huang., "Targeting cancer cells by ROS-mediated mechanisms: a radical therapeutic approach?," Nature reviews Drug discovery, vol. 8, no. 7, p. 579-591, 2009.
[40] S. Pal, and Y. K. Tak, and J. M. Song, "Does the antibacterial activity of silver nanoparticles depend on the shape of the nanoparticle? A study of the gram-negative bacterium Escherichia coli.," Applied and environmental microbiology, vol. 73, no. 6, p. 1712-1720, 2007.
[41] M. Hunger, and J. Weitkamp., "In situ IR, NMR, EPR, and UV/Vis Spectroscopy: Tools for New Insight into the Mechanisms of Heterogeneous Catalysis," Angewandte Chemie International Edition, vol. 40, no. 16, p. 2954–2971, 2001.
[42] Brennan, NF., "University of Pretoria etd," 2006. [Online]. Available: http://repository.up.ac.za/bitstream/handle/2263/30517/04chapter4.pdf?sequence=5&isAllowed=y.
[43] [Online]. Available: https://www.phi.com/surface-analysis-techniques/xps-esca.html.
[44] H. Rehme E. Fuchs, H. Oppolzer. Particle Beam Microanalysis. Fundamentals, Methods and Applications. Wiley-VCH, 1991.
[45] [Online]. Available: http://www.seallabs.com/how-xps-works.html.
[46] K. M. Lang, and D. A. Hite, and R. W. Simmonds, and J. M. Martinis., "Conducting atomic force microscopy for nanoscale tunnel barrier characterization," Review of Scientific Instruments, vol. 75, no. 8, p. 2726–2731, 2004.
[47] Sudha, P. D. C., Pharmaceutical Analysis, Pearson, 2013.
[48] H. Teramoto, and K.-i. Nakajima , and C. Takabayashi., "Chemical Modification of Silk Sericin in Lithium Chloride/Dimethyl Sulfoxide Solvent with 4-Cyanophenyl Isocyanate," Biomacromolecules, vol. 5, no. 4, p. 1392-1398, 2004.
[49] J. Kong, and S. Yu., "Fourier Transform Infrared Spectroscopic Analysis of Protein Secondary Structures," Acta Biochimica et Biophysica Sinica, vol. 39, no. 8, p. 549–559, 2007.
[50] Barth, A., "Infrared spectroscopy of proteins," Biochimica et Biophysica Acta , vol. 1767, no. 9, p. 1073–1101, 2007.
[51] S. Si, and T. K. Mandal., "Tryptophan-Based Peptides to Synthesize Gold and Silver Nanoparticles:A Mechanistic and Kinetic Study," Chemistry - A European Journal, vol. 13, no. 11, p. 3160 – 3168, 2007.
[52] D. A. Malencik, and S. R. Anderson, "Dityrosine as a product of oxidative stress and fluorescent probe," Amino Acids, vol. 25, no. 3, p. 233–247, 2003.
[53] Mohan, J., Organic Spectroscopy: Principles and Applications, CRC Press, 2004.
[54] G. Li, and D. He, and Y. Qian, and B. Guan, and S. Gao, and Y. Cui , and K. Yokoyama, and L. Wang "Fungus-Mediated Green Synthesis of Silver Nanoparticles Using Aspergillus terreus," International Journal of Molecular Sciences, vol. 13, no. 1, p. 466-476, 2012.

[55] D. Gupta, and A. Agrawal, and A. Rangi, "Extraction and characterization os silk sericin", Indian Journal of Fibre & Textile Research, vol. 39, no. 4, p. 364–372, 2014.
[56] A. Dikon, and, R. Olah., "Silver Coated Foley Catheters – Initial Cost Is Not the Only Thing To Consider," American Journal of Infection Control, vol. 34, no. 5, p. 39-40, 2006.
[57] DuPont, [Online]. Available: http://www.dupont.com/products-and-services/electronic-electrical-materials/printed-electronics.html.
[58] V. Joseph, and S. Gunasekaran"Photoconductivity and dielectric studies of potassium pentaborate crystal (KB5)," Bulletin of Materials Science, vol. 26, p. 383-386, 2003.
[59] H. Nakanishi, and K. J. M. Bishop, and B. Kowalczyk, and A. Nitzan, and E. A. Weiss, and K. V. Tretiakov, and M. M. Apodaca, and R. Klajn, and J. F. Stoddart, and B. A. Grzybowski., "Photoconductance and inverse photoconductance in films of functionalized metal nanoparticles," Nature , vol. 460, p. 371-375, 2009.
[60] [Online] http://www.lenntech.com/periodic/elements/mn.htm#ixzz3bqYZlyXJ.
[61] J. Buschmann, and M. Berg, and C. Stengel, and L. Winkel, and M. L. Sampson, and P.T. K. Trang, and P. H. Viet., "Contamination of drinking water resources in the Mekong delta floodplains: Arsenic and other trace metals pose serious health risks to population," Environment International, vol. 34, no. 6, p. 756–764, 2008
[62] K.M. Powers, and T. Smith-Weller, and G.M. Franklin, and W.T. Longstreth Jr., and P.D. Swanson, and H. Checkoway., "Parkinson's disease risks associated with dietary iron, manganese, and other nutrient intakes," Neurology, vol. 60, no. 11, p. 1761-1766, 2010.
[63] López-Lázaro, M., "Dual role of hydrogen peroxide in cancer: possible relevance to cancer chemoprevention and therapy," Cancer Letters, vol. 252, no. 1, p. 1-8, 2007.
[64] C. Hanley, and J. Layne, and A. Punnoose, and K. M. Reddy, and I. Coombs, and A. Coombs, and K. Feris, and D. Wingett., "Preferential killing of cancer cells and activated human T cells using ZnO nanoparticles," Nanotechnology, vol. 19, no. 29, 2008.
[65] M. J. Akhtar, and M. Ahamed, and S. Kumar, and MA M. Khan, and J. Ahmad, and S. A. Alrokayan., "Zinc oxide nanoparticles selectively induce apoptosis in human cancer cells through reactive oxygen species," International Journal of Nanomedicine, vol. 7, p. 845-857, 2012.
[66] W. Lin, and Y. Xu, and C.-C. Huang, and Y. Ma, and K. B. Shannon, and D.-R. Chen, and Y.-W. Huang., "Toxicity of nano- and micro-sized ZnO particles in human lung epithelial cells," Journal of Nanoparticle Research, vol. 11, no. 1, p. 25–39, 2009.
[67] J. Sosna, and S. Voigt, and S. Mathieu, and A.Lange, and L. Thon, and P. Davarnia, and T. Herdegen, and A. Linkermann, and A. Rittger, and F. Ka-Ming Chan, and D. Kabelitz, and S. Schütze, and D. Adam, TNF-induced necroptosis and PARP-1-mediated necrosis represent distinct routes to programmed necrotic cell death," Cellular and molecular life sciences, vol. 71, no. 2, p. 331-348, 2014.

Acknowledgment

I would like to express my profound appreciation firstly to my doctor father, Prof. Dr.-Ing. Mady Elbahri, who has given me the opportunity to work in his group as well as for his scientific supervision. With your continuous support, enthusiasm and innovative ideas this work develop and mature.

Special thanks to Prof. Dr. rer. nat. Dieter Adam and his group (Institut für Immunologie, Universitätsklinikum Schleswig-Holstein) for their cooperation in the investigation of zincoxide nanoparticles in cancer treatment . It was a pleasure and an honor to work with you. Thank you for your supervision and all your efforts.

Furthermore, I am thankful to Dr. Ramzy Abdelaziz, Dr. Mehdi Keshavarz Hedayati, Dr. Ahnaf Usman Zillohu, Dr. Shahin Homaeigohar, for their help, scientific discussion, unconditional support in my experimental work and friendship during my study. The discussions in between our experiments and the office chats were always fun. I'm grateful to you all.

I would also like to sincerely thank group of Multicomponent Materials, especially Prof. Dr. Franz Faupel, Dipl.-Ing. Stefan Rehders, and Dr. Thomas Strunkus for their support and help during my studies. Moreover, I would like to thank the group of Synthesis and Real Structure for TEM investigations. I am also thankful to group of Biocompatible nanomaterials for AFM measurements. For electrical measurements and proof reading I would like to thank Jan Pöhls. The thesis would be missing without your help. I appreciate your support.

I would also thank to M.Sc. Fabian Schütt and M.Sc. Claudia Tillack for their supportive work. It was a pleasure to work with you.

Most important of all I would like to thank my family especially my husband, my parents and my aunt for their extreme support, patient, and unconditional love. I experienced many difficulties within the last years, however, having my family support at all times gave me the courage and motivation to keep going. I love you all very much.

As last, I dedicate this thesis to my son Karim. Since the day he came to my life I was blessed. I love you the most.

List of Abbreviations

^{o}C	Degree Celsius
μg……	Microgram
μm……..	Micrometer
μL……..	Microliter
3D……..	Three dimensional
AFM……..	Atomic force microscopy
a.u. …….....	Arbitrary unit
BNC…….....	Bionanocomposite
dH_2…….....	Deionized water
DNA……..	Deoxyribonucleic acid
Exp……	Experiment
EmWl…….....	Emission wavelength
ExWl…….....	Excitation wavelength
FTIR…….....	Fourier transform infrared spectroscopy
g……..	Grams
kDa…….	Kilo Dalton
keV…….	Kilo electron volt
L……	Liter
LSPR…….....	Localized surface plasmon resonance
M……	Molar
mg…….....	Miligram
min…….....	Minutes
mL…….....	Mililiter
mm…….....	Milimeter
mM…….....	Milimolar
NAD…….....	Nicotinamide-adenine-dinucleotide
NAD+…….....	Oxidized form of nicotinamide-adenine-dinucleotide
NADH…….....	Reduced form of nicotinamide-adenine-dinucleotide
nA…….....	Nanoampere
NIR.....	Near-infrared
nm…….....	Nanometer
ns.....	Nanoseconds
NP…….....	Nanoparticle
Phe…….....	Phenylalanine
ppb…….....	Parts per billion
ppm…….	Parts per million
ppt …….....	Parts per trillion
PS…….....	Polystyrene
ROS……	Reactive oxygen species
rpm…….....	Rotation per minute
RT…….....	Room temperature
s…….....	Seconds
SEM…….....	Secondary electron microscopy
TEM…….....	Transmission electron microscopy

Trp…….....	Tryptophane
Tyr…….....	Tyrosine
kDa…….....	Kilo Dalton
UV-Vis…….....	Ultraviolet–visible
XPS…….....	X-ray photoelectron spectroscopy
wt%…….....	Weight percent

Eidesstattliche Erklärung

Ich versichere an Eides Statt durch meine Unterschrift, dass die vorliegende Arbeit nach Inhalt und Form meine eigene Arbeit ist. Diese Arbeit ist unter Einhaltung der Regeln guter wissenschaftlicher Praxis der Deutschen Forschungsgemeinschaft entstanden. Alle Textpassagen, die wörtlich oder dem Sinn nach auf Publikationen oder Vorträgen anderer Autoren beruhen, ebenso Zeichnungen, Skizzen und andere bildliche Darstellungen, die nicht von mir stammen, sind als solche kenntlich gemacht. Ich versichere außerdem, dass ich keine andere Literatur, als die hier angegebene verwendet habe. Diese Arbeit wurde bisher keiner anderen Prüfungsbehörde vorgelegt und auch als ganzes noch nicht veröffentlicht. Auszüge dieser Arbeit sind in wissenschaftlichen Zeitschriften erschienen, wie der Liste der eigenen Publikationen entnommen werden kann.

25.07.2016
Straelen

Duygu Disci-Zayed